Multiplicity dependence of light-flavor hadron production in pp collisions at root s=7 TeV

The ALICE collaboration

2019-02-08

Multiplicity dependence of light-flavor hadron production in pp collisions at $\sqrt{s} = 7\,\mathrm{TeV}$

S. Acharya *et al.*[*]

(ALICE Collaboration)

Comprehensive results on the production of unidentified charged particles, $\pi^{\pm}$, $\mathrm{K}^{\pm}$, K^0_S, $\mathrm{K}^*(892)^0$, p, $\overline{p}$, $\phi(1020)$, Λ, $\overline{\Lambda}$, Ξ^-, $\overline{\Xi}^+$, Ω^-, and $\overline{\Omega}^+$ hadrons in proton-proton (pp) collisions at $\sqrt{s} = 7$ TeV at midrapidity ($|y| < 0.5$) as a function of charged-particle multiplicity density are presented. In order to avoid autocorrelation biases, the actual transverse momentum (p_T) spectra of the particles under study and the event activity are measured in different rapidity windows. In the highest multiplicity class, the charged-particle density reaches about 3.5 times the value measured in inelastic collisions. While the yield of protons normalized to pions remains approximately constant as a function of multiplicity, the corresponding ratios of strange hadrons to pions show a significant enhancement that increases with increasing strangeness content. Furthermore, all identified particle-to-pion ratios are shown to depend solely on charged-particle multiplicity density, regardless of system type and collision energy. The evolution of the spectral shapes with multiplicity and hadron mass shows patterns that are similar to those observed in p-Pb and Pb-Pb collisions at Large Hadron Collider energies. The obtained p_T distributions and yields are compared to expectations from QCD-based pp event generators as well as to predictions from thermal and hydrodynamic models. These comparisons indicate that traces of a collective, equilibrated system are already present in high-multiplicity pp collisions.

I. INTRODUCTION

Recently, several collective phenomena have been observed in high-multiplicity pp and p-Pb collisions that are reminiscent of observations attributed to the creation of a medium in thermal and kinematic equilibrium in Pb-Pb collisions. In p-Pb collisions, these include the observation of double-ridge structures on the near and away sides in two-particle correlation studies [1], nonvanishing v_2 coefficients in multiparticle cumulant studies [2], mass-dependent hardening of identified particle p_T spectra [3–5], and consistency of integrated particle yield ratios with thermal model expectations at high multiplicities [6].

While double-ridge structures have already been observed in high-multiplicity pp collisions [7], a comprehensive study of identified-particle hadrochemistry as well as of the corresponding kinematics after hadronization has not yet been performed in these collisions: Such a study is the main topic covered in this paper. The investigation of mass-dependent effects as expected within a hydrodynamic evolution scenario requires the measurement of several particle species such as the ones presented here and relies on the excellent particle-identification capabilities provided by the ALICE detector.

While similarities in the production of light-flavor hadrons between p-Pb and Pb-Pb collisions at comparable event multiplicities have been discussed previously [4,6], the measurements presented here allow a unique comparison of the observables with several QCD-inspired event generators such as PYTHIA [8] and EPOS [9]. Traditionally, bulk particle production in heavy-ion collisions is described on the basis of equilibrium many-body theories such as hydro- and thermodynamics (see, for instance, Refs. [10,11] and references therein). The continuous transition of light-flavor hadron measurements from pp to p-Pb and Pb-Pb collisions as a function of event multiplicity thus links the dynamic production of particles in individual $2 \rightarrow 2$ QCD parton-parton scattering processes and subsequent hadronization as an underlying equilibration mechanism to a thermodynamic description of the system.

In a recent paper [12], the ALICE Collaboration reported the multiplicity-dependent enhancement of strange (K^0_S, Λ, and $\overline{\Lambda}$) and multistrange (Ξ^-, Ω^-, $\overline{\Xi}^+$, and $\overline{\Omega}^+$) particle production in pp collisions at $\sqrt{s} = 7$ TeV. In this paper, those results are complemented by the measurement of $\pi^{\pm}$, $\mathrm{K}^{\pm}$, p, $\overline{p}$, $\mathrm{K}^*(892)^0$, and $\phi(1020)$, as well as by an extended discussion on p_T-differential and p_T-integrated particle ratios and model comparisons. For the sake of brevity, in this work, $(\pi^+ + \pi^-)$ and $(\mathrm{K}^+ + \mathrm{K}^-)$ will be denoted by $\pi^{\pm}$ and $\mathrm{K}^{\pm}$, while p refers to $(p + \overline{p})$ unless otherwise stated. In addition, $(\Xi^- + \overline{\Xi}^+)$ and $(\Omega^- + \overline{\Omega}^+)$ will be denoted by Ξ and Ω, while Λ refers solely to the particle and not the antiparticle unless otherwise stated. Finally, $[\mathrm{K}^*(892)^0 + \overline{\mathrm{K}^*(892)}^0]$ and $\phi(1020)$ will be denoted simply by K^{*0} and ϕ throughout this document. The paper is organized as follows. In Sec. II, the

---

[*]Full author list given at the end of the article.

details of the analysis techniques and the event classification are described. The results are given in Sec. III, in which the transverse momentum spectra as well as the extraction of the p_T-integrated yields and average transverse momenta are presented. Detailed model comparisons and an interpretation of the results are presented and discussed in Sec. IV.

II. ANALYSIS

For this analysis, data collected by ALICE in the Large Hadron Collider (LHC) pp run of the year 2010 are used. In total, the analysis is based on up to 281 million minimum-bias events, corresponding to an integrated luminosity of $4.5 \, \text{nb}^{-1}$. A detailed description of the ALICE apparatus and of its performance can be found in Refs. [13,14]. The main subdetectors used in this analysis are the inner tracking system (ITS) [15,16], the time projection chamber (TPC) [17], the time-of-flight detector (TOF) [18], and the V0 scintillator hodoscopes [19]. All tracking detectors are positioned inside a magnetic field $B = 0.5$ T.

The innermost barrel detector is the ITS, consisting of six cylindrical layers of high-resolution silicon tracking detectors using three different technologies. The two innermost layers are based on silicon pixel technology (SPD) with digital readout. The four outer layers, made of drift (SDD) and strip (SSD) detectors provide analog readout and thus allow for particle identification via specific energy loss. The ITS, used as a standalone tracker, enables the reconstruction and identification of low-momentum particles down to 100 MeV/c that do not reach the TPC.

The TPC is a large cylindrical drift detector of radial and longitudinal dimensions of approximately $85 \, \text{cm} < r < 250 \, \text{cm}$ and $-250 \, \text{cm} < z < 250 \, \text{cm}$, respectively. As the main tracking device, it thus provides full azimuthal acceptance for tracks in the pseudorapidity region $|\eta| < 0.9$. In addition, it provides particle identification via the measurement of the specific energy loss dE/dx. At low transverse momenta ($p_T \lesssim 1.0 \, \text{GeV}/c$), the dE/dx resolution of 5.2% for a minimum ionizing particle allows a track-by-track identification, while at high transverse momenta ($p_T \gtrsim 2.0 \, \text{GeV}/c$) the overlapping energy losses can still be statistically distinguished using a multi-Gaussian fit to the dE/dx distributions.

Further outward in radial direction from the beam pipe and located at a radius of approximately 4 m, the TOF measures the time-of-flight of the particles, providing particle identification over a broad range at intermediate transverse momenta ($0.5 \lesssim p_T \lesssim 2.7 \, \text{GeV}/c$). It is a large-area array of multigap resistive plate chambers with an intrinsic time resolution of 50 ps. The total time resolution includes contributions from the start time determination and amounts to about 120 ps in pp collisions. As described in detail in Ref. [20], the start time contribution to the total time resolution improves with increasing number of hits in the TOF in a given event, thus leading to a slight dependence on the event multiplicity and results in a total time resolution of about 100 ps for the highest multiplicities under study.

The V0 detectors are two scintillator hodoscopes that are located on either side of the interaction region at $z = 3.3$ m and $z = -0.9$ m, respectively. They cover the pseudorapidity region $2.8 < \eta < 5.1$ and $-3.7 < \eta < -1.7$ in full azimuth and are employed for triggering, background suppression, and event-class determination.

Measurements of unidentified and identified primary particles are reported. Primary particles are defined as any hadron with a mean proper lifetime that is of at least 1 cm/c either produced directly in the interaction or emerging from decays of particles with lifetime shorter than 1 cm/c and excluding particles from interactions with the detector material [21]. The criteria for the selection of primary tracks for $\pi^{\pm}$, $K^{\pm}$, p, and $\overline{p}$ as well as for the decay products of K^{*0} and ϕ follow the procedures described in Ref. [22]. All measurements are corrected for detector acceptance and reconstruction efficiency using Monte Carlo events generated with PYTHIA6 PERUGIA 0 [23,24] and propagated through the full ALICE geometry with GEANT3 [25]. These events are then reconstructed using the same techniques employed in the case of real data. The corresponding detector acceptance and reconstruction efficiencies are found to be multiplicity independent within 1% and thus the multiplicity-integrated values are used for all event classes to minimize statistical fluctuations.

A. Event selection and classification

The data were collected using a minimum-bias trigger requiring a hit either in the A or C side of the V0 (denoted in what follows as V0A or V0C, respectively) or in the SPD, in coincidence with the arrival of proton bunches from both directions. Contamination from beam-gas events is removed offline by using timing information from the V0, which has a time resolution better than 1 ns. Events in which pileup or beam-gas interactions occurred are also rejected by exploiting the correlation between the number of pixel hits and the number of SPD tracklets. Interactions used for the data analysis are further required to have a reconstructed primary vertex within $|z| < 10$ cm, where z is in the direction of the beam. Events containing more than one reconstructed vertex are tagged as pileup occurring within the same bunch crossing and discarded for the analysis, with up to 10% of all events being tagged in the highest multiplicity event class considered for analysis. The pileup tagging was estimated to be efficient enough so that the residual pileup remaining in the analyzed event sample is of no more than 10^{-4} to 10^{-2} for the lowest and highest multiplicity classes, respectively. The systematic uncertainty associated to pileup rejection was estimated to be smaller than 1% and is therefore not a dominant source of uncertainty for any of the analyses reported here.

The measurements shown here correspond to an event class (INEL > 0) in which at least one charged particle is produced in the pseudorapidity interval $|\eta| < 1$ with respect to the beam, corresponding to about 75% of the total inelastic cross section. In order to study the multiplicity dependence of light-flavor hadron production, the sample is divided into event classes based on the total charge deposited in both of the V0 detectors (V0M amplitude). The V0M amplitude is found to be linearly proportional to the total number of charged particles produced in the pseudorapidity window corresponding to the acceptance of the V0 scintillators.

TABLE I. Event multiplicity classes used in the analysis, their corresponding fraction of the INEL > 0 cross section ($\sigma/\sigma_{INEL>0}$), and their corresponding $\langle dN_{ch}/d\eta \rangle$ in $|\eta| < 0.5$. The value of $\langle dN_{ch}/d\eta \rangle$ in the inclusive INEL > 0 class is 5.96 ± 0.23. The uncertainties are the quadratic sum of statistical and systematic contributions. Table from Ref. [12].

Multiplicity class	I	II	III	IV	V
$\sigma/\sigma_{INEL>0}$	0–0.95%	0.95–4.7%	4.7–9.5%	9.5–14%	14–19%
$\langle dN_{ch}/d\eta \rangle$	21.3 ± 0.6	16.5 ± 0.5	13.5 ± 0.4	11.5 ± 0.3	10.1 ± 0.3
Multiplicity class	VI	VII	VIII	IX	X
$\sigma/\sigma_{INEL>0}$	19–28%	28–38%	38–48%	48–68%	68–100%
$\langle dN_{ch}/d\eta \rangle$	8.45 ± 0.25	6.72 ± 0.21	5.40 ± 0.17	3.90 ± 0.14	2.26 ± 0.12

Table I also lists the average charged-particle pseudorapidity densities $\langle dN_{ch}/d\eta \rangle$ within $|\eta| < 0.5$ for the different event multiplicity classes. The relative standard deviations of the corresponding distributions range from 68% to 30% of the average $\langle dN_{ch}/d\eta \rangle$ for the event class with the lowest average multiplicity to the one with the highest, respectively. These are obtained based on the reconstruction of SPD tracklets which have an acceptance of $p_T \gtrsim 50$ MeV/c. The measurement has been fully corrected for acceptance, tracking, and vertexing efficiency as well as for contamination from secondary particles and combinatorial background. Further details can be found in Refs. [26,27]. In addition, all quantities reported in this work are corrected for event detection efficiencies using a data-driven unfolding method. This correction is negligible for high-multiplicity event classes but is of up to ∼13% in multiplicity class X. The resulting percentages of the total INEL > 0 cross section, $\sigma/\sigma_{INEL>0}$, are also reported in Table I. These values are reported after event detection efficiency corrections and do not match the integer boundaries that were used in analysis; e.g., high-multiplicity event classes such as I and II were selected as 0–1% and 1–5% for analysis but event losses at low-multiplicity compress these fractions into 0–0.95% and 0.95–4.7% of the true INEL > 0 cross section. The analysis-level selection percentiles have been omitted as they are detector-dependent quantities.

In previous studies, event classification was based on midrapidity charged-particle densities [27–29], as opposed to the forward and backward pseudorapidity-based selection utilized in this work. This choice is motivated by the fact that performing multiplicity selection and data analysis in the same pseudorapidity range may lead to autocorrelation biases and unphysical results. More specifically, hadrochemistry is significantly altered by selection biases, as exemplified by the progression of charged and neutral kaon abundances with multiplicity. If midrapidity-based selections were used, the integrated yields of $K^\pm$ for high-multiplicity events would be higher than the ones for K^0_S because of the requirement of high charged-particle yields in the same pseudorapidity range. Conversely, if selection is performed with charged-particle yields in a different pseudorapidity range than the one in which $K^\pm$ and K^0_S production rates are measured, similar amounts of charged and neutral kaons would be found across multiplicity, as expected due to their similar masses. This can be readily tested in Monte Carlo simulations, as shown, for instance, in Fig. 1, where the charged and neutral kaon yields in pp collisions simulated with the PYTHIA8 event generator using the Monash 2013 tune [8,30] are studied as a function of either midrapidity or forward or backward pseudorapidity charged-particle multiplicity. A significant bias toward charged kaons is observed in the former case, while the latter
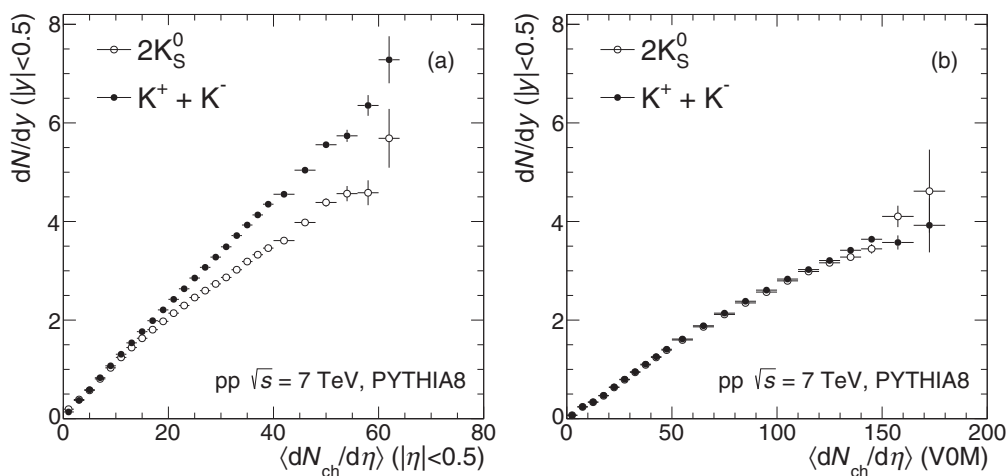

FIG. 1. Multiplicity dependence of charged and neutral kaon yields obtained using (a) midpseudorapidity charged-particle multiplicities ($|\eta| < 0.5$) and (b) the charged-particle multiplicities within the pseudorapidity range corresponding to the V0A and V0C detectors (denoted by V0M, corresponding to $-3.7 < \eta < -1.7$ and $2.8 < \eta < 5.1$) in PYTHIA8 simulations of inelastic pp collisions at $\sqrt{s} = 7$ TeV.

selection preserves the expected neutral-to-charged kaon ratio of approximately unity.

This discrepancy for charged and neutral kaons is understood to be a consequence of performing selections on charged-particle multiplicities whose probability distributions exhibit a rapid decrease and have low average values. Under such circumstances, any multiplicity selections are likely to isolate fluctuations of charged-particle yields in the reference region of phase space rather than uniformly affecting all particle species regardless of their charge. In the particular case of $K^\pm$ and K^0_S production rates, residual differences in these kaon yields still arise from resonance decay products, given that ϕ mesons decay preferentially into charged kaons. However, Monte Carlo studies show that these different feed-down contributions introduce differences in $K^\pm$ and K^0_S yields of no more than 1–2%, further corroborating the need to take into account the much larger selection-bias effects shown in Fig. 1.

However, while multiplicity selections performed in different phase-space regions will avoid selection biases, they are also naturally susceptible to the mid- to forward or backward pseudorapidity multiplicity correlation, which for small systems is not as strong as for nuclear collisions [31]. This has the consequence that the reach in midrapidity charged-particle densities is restricted in comparison to same-phase-space selections: When selecting high charged-particle multiplicities in forward/backward pseudorapidity detectors, midrapidity $\langle dN_{\mathrm{ch}}/d\eta \rangle$ will eventually saturate, while it will still increase if event selection is performed with detectors at midrapidity. Furthermore, the V0 scintillators that are used in this work for forward or backward charged-particle detection and event classification introduce an imperfect detector response into the analysis. In order to minimize potential biases coming from these factors, all observables are studied as a function of charged-particle density at midrapidity $\langle dN_{\mathrm{ch}}/d\eta \rangle$. By doing so, both $dN_{\mathrm{ch}}/d\eta$ and the variables under study are similarly folded with mid- to forward or backward pseudorapidity multiplicity correlations as well as the detector response within a given event class. This allows comparing results from this study with predictions from models by performing selections on charged-particle production in the acceptance of the V0 and it has been verified that any residual effect because of the finite detector resolution is negligible.

B. Unidentified charged particles

Spectra of positively and negatively charged particles were obtained separately and summed afterward. The differences between the final spectra for particles and antiparticles were found to be around 1.5%. The unidentified charged particles were reconstructed using the combined information from ITS and TPC. The p_T range of the spectra in all multiplicity classes based on the V0M amplitudes is 0.16–40 GeV/c and the pseudorapidity was limited to $|\eta| < 0.5$. This pseudorapidity limit allows a comparison of the charged hadron spectrum with the sum of pions, kaons, and protons analyzed in the rapidity range $|y| < 0.5$ by transforming them to the corresponding pseudorapidity window with the appropriate Jacobian $\frac{\mathrm{d}^2 N}{\mathrm{d}y \mathrm{d}p_T} = \frac{E}{p} \frac{\mathrm{d}^2 N}{\mathrm{d}\eta \mathrm{d}p_T}$ for each p_T interval. This cross-check showed a difference of less than 5%, which is consistent

TABLE II. Main sources and values of the relative systematic uncertainties of the p_T-differential yields for unidentified charged particles. The values are reported for low, intermediate, and high p_T. The contributions that act differently in the various event classes are removed from the total (quadratic sum of all contributions), defining the N_{ch}-independent ones, which are correlated across different multiplicity intervals.

Source	Uncertainty (%)		
p_T (GeV/c)	0.16	3.0	40.0
Correction for secondaries	0.2	0.2	1
Particle composition in secondaries	1.7	1.3	0.8
Material budget	1.5	negl.	negl.
Global tracking efficiency	5	5	5
Particle composition	1.7	2	2
Track selection	4	2.8	7.4
MC event generator	1.1	1.8	2
p_T resolution	negl.	negl.	0.5
Efficiency multiplicity dependence	1	1	1
Total	7.2	6.6	9.6
Total (N_{ch} independent)	6.9	6.3	9.4

within the uncommon systematics with the expected contributions from electrons, muons, and heavier charged baryons that are counted in addition to pions, kaons, and protons in the charged hadron spectrum.

The contribution from secondary particles was calculated in the same manner as described in detail in Sec. II C. The additional corrections based on FLUKA [32,33] for kaons and antiprotons, which are needed for those specific identified particle measurements in order to account for an imperfect description of absorption cross section in the detector material, were found to have negligible impact on the unidentified charged-particle spectra and were therefore not applied.

The systematic uncertainties are summarized in Table II. The multiplicity dependence of the tracking efficiency and the feed-down correction were found to be less than 1% and were included in the final systematic uncertainty. The total systematic uncertainty is p_T dependent, with values around 6–7% up to 20 GeV/c. It reaches 9.6% for the highest p_T bin. The main contributions to the total systematic uncertainty come from the global tracking efficiency (5%) and the parameter variation for the track selection criteria (3–7%). The other sources have a p_T-dependent contribution of less than 2% each. The systematic uncertainties related to the dependence of the reconstruction efficiency on the MC event generator and the particle composition have been studied as described in Ref. [34]. All sources of uncertainty are assumed to be uncorrelated and the total uncertainty was calculated as the quadratic sum of the different contributions. The systematic uncertainty contribution that is uncorrelated across multiplicities was estimated to be 2.1% for all the V0M multiplicity bins over the entire p_T range.

C. Charged pions, kaons, and protons

For the measurement of charged pions, kaons, and protons, several subanalyses are combined for the comprehensive ex-

TABLE III. Overview of p_T ranges used for the combination of the various techniques used for identifying pions, kaons, and protons. Since the true rapidity is not known at reconstruction level, fit-based analyses ("TPC template fits" and "TPC-TOF fits"), which determine the yield of pions, kaons, and protons simultaneously, require an additional η cut.

Analysis	PID technique	p_T range (GeV/c)			(Pseudo)rapidity range
		$\pi^{\pm}$	$K^{\pm}$	$p(\bar{p})$	
ITS stand-alone	n-σ cuts on ITS	0.1–0.6	0.2–0.6	0.3–0.6	$|y| < 0.5$
Bayesian PID	Bayesian probability	0.2–2.5	0.3–2.5	0.5–2.5	$|y| < 0.5$
TPC-TOF	n-σ cuts on TPC and TOF	0.25–1.2	0.3–1.2	0.45–2.0	$|y| < 0.5$
TPC-TOF fits	n-σ fits to TPC and TOF	0.25–2.5	0.3–2.5	0.45–2.7	$|y| < 0.5$ (TPC) $|\eta| < 0.2$ (TOF)
TPC template Fits	TPC dE/dx Template fits		>2.0		$|\eta| < 0.8$

ploitation of the available particle identification (PID) techniques in ALICE. The spectra cover a range from 0.1/0.2/0.3 to 20 GeV/c for $\pi^{\pm}$/$K^{\pm}$/$p(\bar{p})$, respectively, with the exact ranges reported in Table III. Similar approaches were followed in earlier analyses in pp, p-Pb, and Pb-Pb collisions [22,35]. An overview of the individual analyses is presented in Table III. Here, we briefly review the most relevant aspects of previously employed techniques: ITS standalone and TPC-TOF. Additionally, we describe methods which are used for the measurement of p_T spectra of charged kaons, pions, and protons: Bayesian PID, TPC-TOF fits, and TPC template fits.

In the "ITS standalone" technique, the average energy loss in the four outer ITS layers is calculated as a truncated mean. For each particle-mass hypothesis, the distance between the measured and the expected value is calculated in multiples of the standard deviation σ of the measured energy-loss distribution and the particle-mass hypothesis with the smallest value assigned. In contrast to the analysis in the high-track-density environment of central heavy-ion collisions, the contribution of tracks with wrongly assigned signal clusters is negligible even in the highest pp event multiplicity class. In the intermediate-p_T range where a track-by-track identification is feasible, the TPC-TOF analysis identifies particles by requiring that the measured energy-loss signals in the TPC and time of flight in the TOF are within 3σ of the expected value, assuming a specific mass hypothesis. This approach finds its natural limitation toward higher momenta, as the expected energy losses and flight times for different species are insufficiently different to allow for a clear separation. The p_T ranges in which this procedure are applicable are given in Table III. Two alternative methods, namely Bayesian PID and TPC-TOF fits, were employed in order to unfold the measured dE/dx and TOF distributions. The Bayesian method of particle identification for the extraction of the minimum-bias spectra of pions, kaons, and protons is described in detail in Ref. [36]. The *a priori* probabilities used in the Bayesian-approach analysis were extracted from the experimental data for the minimum-bias event sample using an iterative procedure. The influence of different sets of *a priori* probabilities, determined for the lowest and highest

event multiplicity bins, was evaluated and included in the systematic uncertainties. The actual identification of particles is based on the maximum probability method in which the most likely particle type is assigned to the track.

In the TPC-TOF fits method, the energy loss distribution in the TPC is simultaneously fitted by three Gaussian distributions corresponding to charged pions, kaons, and protons in each p_T and multiplicity bin. Similarly, the velocity distribution of the TOF is fitted for all three species simultaneously. In order to guarantee a sufficient separation of the particle species by minimizing the difference between total and transverse momentum p_T, the TOF fits were performed in a narrow η window ($|\eta| < 0.2$) and afterward transformed to the common rapidity window of $|y| < 0.5$ assuming a flat distribution in y. Above a p_T of ~ 2 GeV/c, particle identification can still be achieved statistically, rather than on a track-by-track basis, by fitting the specific energy loss in the relativistic rise region with a multicomponent fit function, as done in the TPC template fits approach. In this method, the measured dE/dx distribution, in which the distributions of several particle species are overlapping, is fitted with a sum of templates (one for each particle type). The templates are extracted in a data-driven procedure from a pure sample of tagged particles of a given type. This pure sample is obtained from weak decay daughter tracks (p and $\bar{p}$ from Λ and $\bar{\Lambda}$ as well as $\pi^{\pm}$ from K_S^0) and tracks identified with the TOF ($\pi^{\pm}$, $K^{\pm}$, p, and $\bar{p}$). After a further strict selection of primary-particle-like topologies, the expected dE/dx response is determined in fine bins of momentum and pseudorapidity. The template for each particle species in a given transverse momentum bin in the rapidity window $|y| < 0.5$ is then obtained by sampling the measured momenta and pseudorapidity values of the tracks in this bin. The individual particle yields are the only free parameters in the fit of the templates to the measured dE/dx distribution.

For all particle species and subanalyses, contamination from secondary particles at low transverse momenta was subtracted in a data-driven approach on the basis of the measured distance of closest approach of the track to the primary vertex in the transverse plane (DCA$_{xy}$), as done in previous

TABLE IV. Main sources and values of the relative systematic uncertainties of the p_T-differential yields of $\pi^\pm$, $K^\pm$, and $p(\overline{p})$. The values are reported for low, intermediate, and high p_T. The contributions that act differently in the various event classes are removed from the total (quadratic sum of all contributions), defining the N_{ch}-independent ones, which are correlated across different multiplicity intervals. The contribution from the global tracking efficiency is common to all analyses except for the ITS standalone (ITSsa).

Common source	Uncertainty (%)								
	$\pi^\pm$			$K^\pm$			$p(\overline{p})$		
p_T (GeV/c)	0.1	3.0	20.0	0.2	2.5	20.0	0.3	4.0	20.0
Correction for secondaries	1	1	1		negl.		4	1	1
Material budget	5		negl.	2		negl.	4		negl.
Hadronic interactions	2	1	1	3	1	1	4(6)	1(1)	1(1)
Global tracking efficiency (incl. track cut variation)		4			4			4	
TOF matching efficiency (Bayes.,TPC-TOF,TPC-TOF fits)		3			6			4	

Specific source	$\pi^\pm$			$K^\pm$			$p(\overline{p})$		
p_T (GeV/c)	0.1		0.6	0.2		0.6	0.3		0.6
ITSsa tracking efficiency	3		3	3		3	3		3
$E \times B$ effect					3				
ITS PID	5		1	5		9	8		6
p_T (GeV/c)	0.2		2.5	0.3		2.5	0.5		2.5
Bayesian PID		1		1		3	1		2
p_T (GeV/c)	0.25		1.2	0.3		1.2	0.45		2.0
TPC-TOF PID		1		1		5		1	
p_T (GeV/c)	0.25		2.5	0.3		2.5	0.45		2.7
TPC-TOF fits PID	1		5	1		10	1		8
p_T (GeV/c)	2.0		20.0	2.0		20.0	2.0		20.0
TPC template fits PID	4		6	10		12	8		13

Total	$\pi^\pm$			$K^\pm$			$p(\overline{p})$		
p_T (GeV/c)	0.1	3.0	20.0	0.2	2.5	20.0	0.3	4.0	20.0
Total	8.4	5.0	7.2	7.5	6.6	12.6	12.3	15.1	13.3
Total (N_{ch} independent)	8.1	4.4	6.9	6.7	6.1	12.2	10.5	13.5	11.5

work [22]. The DCA$_{xy}$ distribution of the selected tracks was fitted with three Monte Carlo templates corresponding to the expected shapes of primary particles, of secondaries from material (including electrons from photon conversions), and of secondaries from weak decays. The procedure was repeated for each p_T and event multiplicity bin and thus takes into account possible differences in the feed-down correction due to a change of the abundances and spectral shapes of weakly decaying strange particles.

The efficiencies obtained for antiprotons and kaons have been additionally corrected based on a comparison of the absorption cross section used in GEANT3 and the more realistic description of hadronic cross sections in FLUKA, as in Refs. [22,37].

The determination of systematic uncertainties follows the procedures established in previous analyses [22,35]. All the considered contributions are summarized in Table IV. Corrections for secondary particles lead to uncertainties of up to

4% for protons and 1% for pions while they are negligible for kaons. The uncertainty in the material budget is of 5% at very low momenta and is related to the energy loss of the particles in the detector material. In addition, inelastic and elastic hadronic scattering processes inside the detector material are described by the transport codes only with limited precision and lead to uncertainties of up to 6% for $\overline{p}$ (for which the respective cross section is largest) at low transverse momenta. The track quality selection criteria and the matching of TPC tracks with ITS hits give rise to a systematic uncertainty of the global tracking efficiency that amounts to 4%, independent of p_T and particle species. The Lorentz force causes shifts of the cluster position in the ITS, pushing the charge in opposite directions depending on the polarity of the magnetic field of the experiment ($E \times B$ effect). In the ITS standalone analysis, the uncertainty related to this effect is estimated by analyzing data samples collected with opposite magnetic field polarities, for which a difference of 3% is observed. For those

subanalyses (Bayesian PID, TPC-TOF, TPC-TOF fits) that require in addition that the track under study is matched to a hit in the TOF, an additional uncertainty of 3%/6%/4% is taken into account for pions, kaons, and protons, respectively. Following the approach presented in Ref. [35], this matching efficiency uncertainty was estimated by repeating the analysis separately for those regions in azimuth in which modules of the transition radiation detector were already present in 2010 and for those in which they were not yet installed.

All subanalyses were found to be in agreement in the overlapping p_T ranges within the uncorrelated part of their respective systematic uncertainties. The final combined spectrum for each particle species was then obtained by calculating the average over all subanalyses using the uncorrelated part of their systematic errors as weights [38]. The uncertainties originating from common sources were then added in quadrature to each other and to the uncertainty attributed to the specific particle identification methods. The systematic uncertainty contribution that is uncorrelated across multiplicities was estimated to be ~4–8%, ~6–12%, and ~10–14% for $\pi^\pm$, $K^\pm$, and p, respectively, for all V0M multiplicity bins.

D. Weakly decaying strange hadrons

The strange hadrons K_S^0, Λ, $\overline{\Lambda}$, Ξ^-, $\overline{\Xi}^+$, Ω^-, and $\overline{\Omega}^+$ are reconstructed at midrapidity ($|y| < 0.5$) via their characteristic weak decay topology in the channels [38]

$$
\begin{aligned}
&K_S^0 \to \pi^+ + \pi^-, & \mathrm{BR} &= (69.20 \pm 0.05)\%, \\
&\Lambda(\overline{\Lambda}) \to p\,(\overline{p}) + \pi^-\,(\pi^+), & \mathrm{BR} &= (63.9 \pm 0.5)\%, \\
&\Xi^-\,(\overline{\Xi}^+) \to \Lambda\,(\overline{\Lambda}) + \pi^-\,(\pi^+), & \mathrm{BR} &= (99.887 \pm 0.035)\%, \\
&\Omega^-\,(\overline{\Omega}^+) \to \Lambda\,(\overline{\Lambda}) + K^-\,(K^+), & \mathrm{BR} &= (67.8 \pm 0.7)\%.
\end{aligned}
$$

Charged-particle tracks are selected on the basis of compatibility of their energy loss in the TPC with the expected losses under the pion, kaon, and proton mass hypotheses. They are then combined into weak decay candidates following the topology of a V-shaped decay for K_S^0, Λ, and $\overline{\Lambda}$ (denoted "V0" decays) and a combination of a V0 decay and one additional charged track for Ξ^-, $\overline{\Xi}^+$, Ω^-, and $\overline{\Omega}^+$ (denoted "cascade" decays). In addition to several geometrical criteria on the arrangement of decay daughter tracks, K_S^0, Λ, and Ω^- candidates are required to have a calculated mass that is incompatible with other species that decay in a similar topological arrangement, which are Λ, K_S^0, and Ξ^-, respectively. This selection is commonly denoted as "competing decay rejection" and the exact numerical value depends on the invariant mass resolution for the competing particle species. Furthermore, candidates whose proper lifetimes are unusually large for their expected species are also rejected to avoid combinatorial background from interactions with the detector material. The selection criteria used to define V0 and cascade decay candidates are listed in Tables V and VI, respectively.

Particle yields are calculated in p_T and event multiplicity intervals by extracting the relevant signals from invariant-mass distributions as done in previous work [4,6,39]. Figure 2 shows the invariant-mass distributions of K_S^0 (top left), Λ (top right), Ξ^- (bottom left), and Ω^- (bottom right) in selected transverse momentum ranges for the corresponding highest

TABLE V. Selection criteria parameters utilized in the K_S^0, Λ, and $\overline{\Lambda}$ analyses presented in this work. If a criterion for Λ and K_S^0 differs, the criterion for the Λ hypothesis is given in parentheses. The acronym DCA stands for "distance of closest approach" and PV denotes "primary event vertex." The pointing angle θ is the angle between the momentum vector of the reconstructed V0, and the line segment bound by the decay and primary vertices and R_{2D} denotes the transverse distance from the detector center.

V0 selection criterion	Value
DCA ($h^\pm$ to PV)	>0.06 cm
DCA (h^- to h^+)	<1.0 standard deviations
Fiducial volume (R_{2D})	>0.5 cm
V0 pointing angle	$\cos\theta_{V0} > 0.97\ (0.995)$
Proper lifetime	$<20\ (30)$ cm/c
Competing V0 rejection window	$\pm 5(10)$ MeV/c^2

V0M event multiplicity classes in pp collisions at $\sqrt{s} = 7$ TeV.

Approximately 20% of the measured Λ ($\overline{\Lambda}$) signals are from Ξ^- ($\overline{\Xi}^+$) and Ξ^0 ($\overline{\Xi}^0$) decays. These feed-down contributions were subtracted using a data-driven approach in which the measured Ξ^- ($\overline{\Xi}^+$) spectra are used as input and a simulation is used to evaluate the fraction of reconstructed Λ ($\overline{\Lambda}$) coming from Ξ^- ($\overline{\Xi}^+$) decays. Since production rates of Ξ^0 and $\overline{\Xi}^0$ have not been measured, their contribution

TABLE VI. Selection criteria for V0 (Λ) from cascades, and cascades ($\Xi^\pm$ and $\Omega^\pm$) presented in this work. If a criterion for $\Xi^\pm$ and $\Omega^\pm$ finding differs, the criterion for $\Omega^\pm$ hypothesis is given in parentheses. DCA stands for "distance of closest approach" and PV stands for "primary event vertex." The pointing angle θ is the angle between the momentum vector of the reconstructed V0 or cascade and the line segment bound by the decay and primary vertices and R_{2D} denotes the transverse distance from the detector center. The cascade track curvature is neglected, and τ refers to the average lifetime for the two different cascade species.

V0 from cascade selection criterion	Value
DCA (baryon to PV)	>0.03 cm
DCA (meson to PV)	>0.04 cm
DCA (h^- to h^+)	<1.5 standard deviations
Λ mass (m_{V0})	$1.108 < m_{V0} < 1.124$ GeV/c^2
Fiducial volume (R_{2D})	$>1.2\ (1.1)$ cm
V0 pointing angle	$\cos(\theta_{V0}) > 0.97$
Cascade finding criterion	**Value**
DCA (bachelor to PV)	>0.04 cm
DCA (V0 to PV)	>0.06 cm
DCA ($\pi^\pm$ ($K^\pm$) to V0)	<1.3 cm
Fiducial volume (R_{2D})	$>0.6\ (0.5)$ cm
Cascade pointing angle	$\cos(\theta_{casc}) > 0.97$
Proper lifetime	$<3c\tau$
Competing cascade rejection window ($\Omega^\pm$ only)	± 8 MeV/c^2

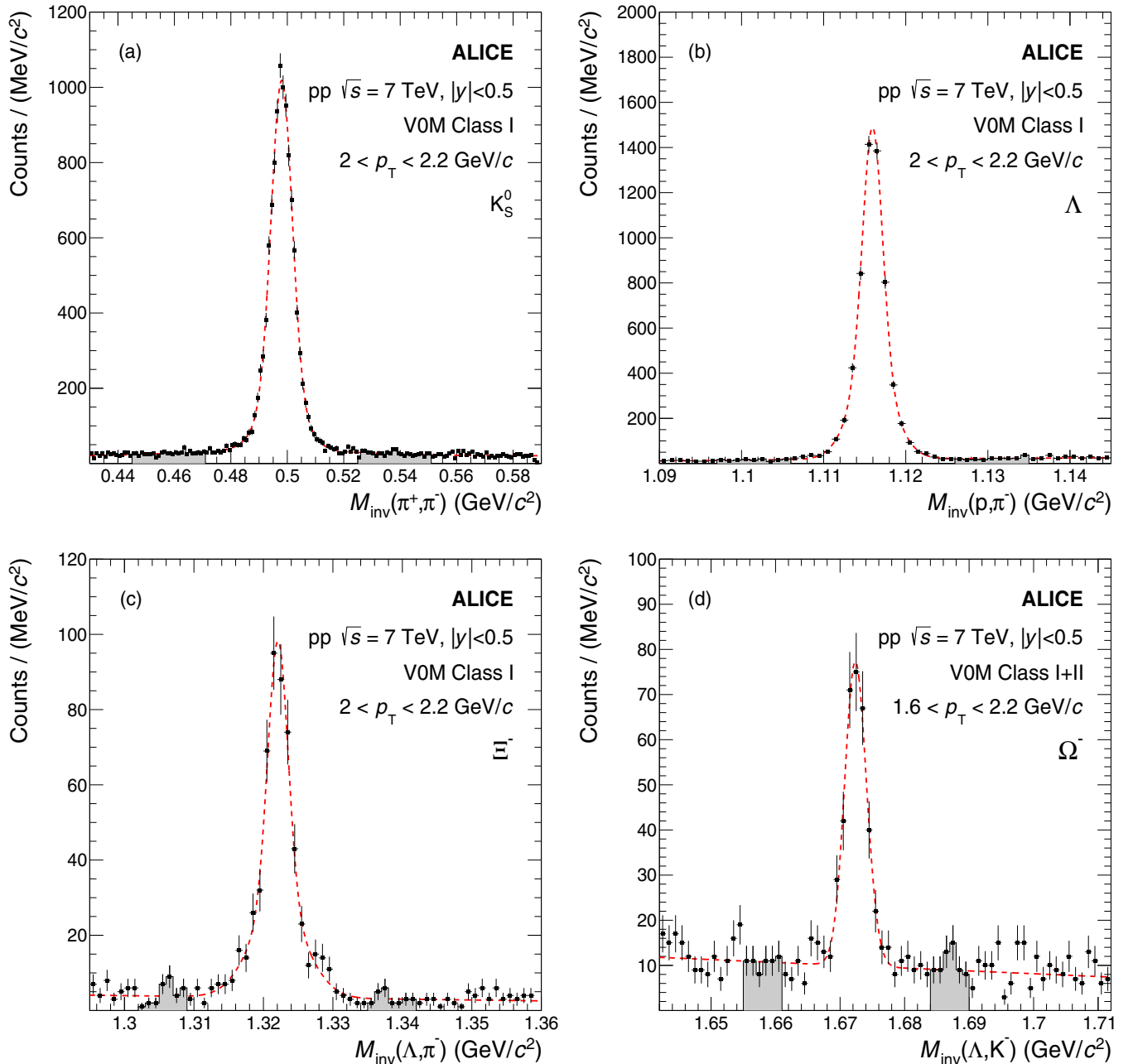FIG. 2. Invariant-mass distributions of (a) K_S^0, (b) Λ, (c) Ξ^-, and (d) Ω^- (bottom right) decay candidates in selected p_T ranges for the corresponding highest V0M event multiplicity classes in pp collisions at $\sqrt{s} = 7$ TeV. The statistical uncertainties are shown by error bars and the shaded bands on the sides of the peak represent the regions used to estimate the background. The red dashed curves represent fits using a Gaussian peak and a linear background.

is estimated by assuming that they are as abundant as their charged counterparts and that their momentum distributions are identical.

Because in the specific case of the cascade analysis the measurement is performed in large momentum intervals because of the limited amount of data, efficiencies are reweighted in each p_T bin to take into account differences between generated and real data spectral shapes.

Systematic uncertainties for K_S^0, Λ, $\overline{\Lambda}$, Ξ^-, $\overline{\Xi}^+$, Ω^-, and $\overline{\Omega}^+$ are estimated following the procedure described in

Refs. [4,6]. The main sources of systematic uncertainty in these measurements are track selections (up to $\sim$6%), knowledge of detector materials (4%), feed-down from Ξ^- ($\overline{\Xi}^+$) and Ξ^0 ($\overline{\Xi}^0$) for the Λ ($\overline{\Lambda}$) (up to $\sim$4%), and topological selections, which contribute with a $\sim$1–8% uncertainty. The contributions to systematic uncertainties are summarized in Table VII. As in previous work, the study of systematic uncertainties was repeated for all event classes to determine differences in how each contribution affects results from each of these classes.

TABLE VII. Main sources and values of the relative systematic uncertainties (expressed in %) of the p_T-differential yields of K^0_S, $\Lambda(\overline{\Lambda})$, $\Xi^-(\overline{\Xi}^+)$, and $\Omega^-(\overline{\Omega}^+)$. The values are reported for low, intermediate, and high p_T. The contributions that act differently in the various event classes are removed from the total (quadratic sum of all contributions), defining the N_{ch}-independent ones, which are correlated across different multiplicity intervals.

Hadron species	K^0_S			$\Lambda(\overline{\Lambda})$		
p_T range (GeV/c)	0.05	6.2	11.0	0.5	3.7	7.2
Material budget	4.0	4.0	4.0	4.0	4.0	4.0
Transport code		Negligible		1.0	1.0	1.0
Track selection	1.0	5.0	0.8	0.2	5.9	4.3
Topological selection	2.6	1.1	2.3	0.8	0.6	3.2
Particle identification	0.1	0.1	0.1	0.2	0.2	3.0
Efficiency determination	2.0	2.0	2.0	2.0	2.0	2.0
Signal extraction	1.5	1.2	3.6	0.6	0.7	3.0
Proper lifetime	1.3	0.1	0.2	0.3	2.3	0.1
Competing decay rejection	negl.	0.7	1.3	negl.	1.0	6.2
Feed-down correction		not applicable		3.3	2.1	4.3
Total	5.6	6.9	6.4	5.8	8.2	11.2
Common (N_{ch}-independent)	5.0	5.9	4.4	5.4	7.8	9.9
Hadron species	$\Xi^-(\overline{\Xi}^+)$			$\Omega^-(\overline{\Omega}^+)$		
p_T range (GeV/c)	0.8	2.1	5.8	1.2	2.8	4.7
Material budget	4.0	4.0	4.0	4.0	4.0	4.0
Transport code	1.0	1.0	1.0	1.0	1.0	1.0
Track selection	0.4	0.3	2.2	0.8	0.6	4.1
Topological selection	3.1	2.0	4.0	5.0	5.6	8.1
Particle identification	1.0	0.2	1.2	1.1	1.7	3.2
Efficiency determination	2.0	2.0	2.0	2.0	2.0	2.0
Signal extraction	1.5	0.2	1.0	3.2	2.5	2.3
Proper lifetime	0.9	0.1	0.1	2.2	0.7	0.7
Competing decay rejection		not applicable		0.2	4.2	5.2
Feed-down correction		negligible			negligible	
Total	5.9	5.0	6.7	7.9	9.0	12.1
Total (N_{ch} independent)	5.2	4.5	6.2	7.3	8.7	11.6

E. Resonances

The K^{*0} and ϕ mesons are reconstructed at midrapidity $|y| < 0.5$ via their hadronic decay channels into charged particles,

$$K^{*0} \rightarrow \pi^\pm + K^\mp, \quad \text{BR} = (\sim 66.6)\%,$$
$$\phi \rightarrow K^+ + K^-, \quad \text{BR} = (48.9 \pm 0.5)\%.$$

Both the TPC and TOF information are used to identify charged particles as pions or kaons from K^{*0} decays, whereas only TPC information is used to identify charged particles as kaons from decays of ϕ mesons, as in the latter case the combinatorial background is significantly smaller.

Pairs of pions and kaons (pairs of kaons) of opposite charge are considered to obtain the invariant mass distribution of K^{*0} (ϕ) decay candidates. An event mixing technique is used to estimate the combinatorial background. The mixed-event distribution is normalized in the mass region outside of the mass peak, i.e., at $1.1 < M_{\pi K}$ (GeV/c^2) < 1.15 and $1.035 < M_{KK}$ (GeV/c^2) < 1.045 for K^{*0} and ϕ mesons, respectively. The normalized mixed-event distribution is subtracted from the same event unlike-sign distribution to isolate the relevant signals. After mixed-event background subtrac-

tion, each invariant mass distribution is fitted with a Breit-Wigner function (Voigtian function) for the signal and a second-order polynomial for any residual background. The parametrizations for the signal are given in Eq. (1) for the K^{*0} and Eq. (2) for the ϕ meson:

$$\frac{dN}{dM_{\pi K}} = \frac{Y}{2\pi} \times \frac{\Gamma}{(M_{\pi K} - M_0)^2 + \frac{\Gamma^2}{4}}, \tag{1}$$

$$\frac{dN}{dM_{KK}} = \frac{Y}{2\pi} \int \frac{\Gamma}{(M_{KK} - m')^2 + \Gamma^2/4}$$
$$\times \frac{e^{-(m' - M_0)^2/2\sigma^2}}{\sqrt{2\pi}\sigma} dm' \tag{2}$$

where $M_{\pi K}$ and M_{KK} are the reconstructed invariant masses of K^{*0} and ϕ-meson candidates, and M_0, Γ, and Y are the mass, width, and raw yield of the resonances, respectively. The parameter σ represents the mass resolution. Figure 3 shows the invariant mass of π K (KK) in the left (right) panel for $2 < p_T < 2.5$ GeV/c in the V0M event multiplicity class I.

The raw yields are extracted in each p_T bin and event multiplicity interval as done in previous works [5,40,41]. In this
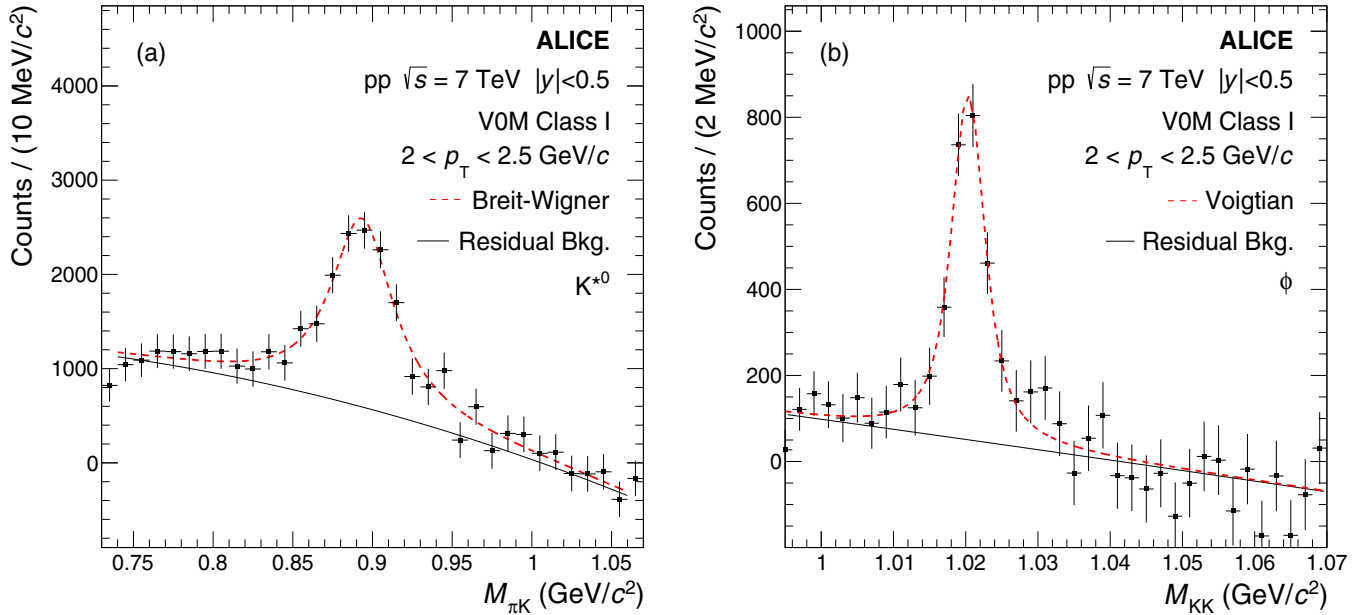
FIG. 3. Invariant mass distributions of π K and KK in the momentum range of $2 < p_T < 2.5$ GeV/c for V0M event multiplicity class I are shown in panels (a) and (b), respectively. The statistical uncertainties are shown by vertical bars. The red dashed curves represent fits to the distributions and the solid curves describe the residual background.

analysis, detector acceptance and reconstruction efficiency are reweighted in each p_T bin to take into account the differences between generated and real data spectral shapes.

The sources of systematic uncertainties for K^{*0} and ϕ-meson production in pp collisions are the TPC-ITS matching efficiency, track selection criteria, PID, yield extraction method, hadronic interaction, and material budget and were evaluated following the same prescription used in previous works [40,41]. The main source of uncertainty for K^{*0} and ϕ comes from the determination of the TPC-ITS track matching efficiency. This contribution has been estimated to be a p_T-independent effect of 3% for charged particles [42], which results in a 6% effect when any two primary tracks are combined in the invariant-mass analysis of K^{*0} and ϕ. For both K^{*0} and ϕ, the uncertainties due to various track selection cuts from low to high p_T are found to be 0.9–3.0% and 1.6–2.4%, respectively. The systematic uncertainty due to the signal extraction includes variations in the fit range, fit function, and normalization range and is of $\sim$5–10% ($\sim$3–9%) from low to high p_T for K^{*0} (ϕ). The uncertainty due to different PID selection methods is estimated to be $\sim$2–4% ($\sim$1–2%) for K^{*0} (ϕ). The knowledge of the material budget for both K^{*0} and ϕ contributes to $\sim$4% and $\sim$6% at low p_T and is negligible at high p_T. The contribution from the estimate of the hadronic interaction cross section in the detector material at low p_T is $\sim$4% ($\sim$6%) for K^{*0} (ϕ) and negligible at high p_T. The total systematic uncertainties for K^{*0} and ϕ are estimated to be about 12% and 10%, respectively. The maximum value of the multiplicity-independent systematic uncertainty is found to be $\sim$8% ($\sim$5%) for K^{*0} (ϕ). The main contributions to the systematic uncertainties are summarized in Table VIII.

The systematic uncertainties were studied independently for all event classes, in order to separate the sources that are multiplicity dependent and uncorrelated across multiplicity bins. In particular, signal extraction and PID are fully uncorrelated sources, whereas global tracking, track cuts, material budget, and hadronic cross sections are correlated among different event multiplicity classes.

III. RESULTS

A. Transverse momentum distributions

The transverse momentum distributions measured at midrapidity for the event classes defined in Table I are shown in Fig. 4 for unidentified charged particles ($|\eta| < 0.5$) and Fig. 5 for $\pi^{\pm}$, K$^{\pm}$, K^0_S, K^{*0}, p, $\overline{p}$, ϕ, Λ, $\overline{\Lambda}$, Ξ^-, $\overline{\Xi}^+$, Ω^-,

TABLE VIII. Main sources and values of the relative systematic uncertainties (expressed in %) of the p_T-differential yields of ϕ and K^{*0} resonances. The values are reported for low, intermediate, and high p_T. The contributions that act differently in the various event classes are removed from the total (quadratic sum of all contributions), defining the N_{ch}-independent ones, which are correlated across different multiplicity intervals.

Hadron species	K^{*0}			ϕ		
p_T (GeV/c)	0.4	3.0	10.0	0.6	3.0	10.0
Global tracking efficiency		6			6	
Signal extraction	5.1	4.6	9.7	3.1	3.2	8.5
Track selection cuts	3.0	2.1	0.9	1.6	1.6	2.4
Particle identification	1.8	2.5	4.0	1.1	1.9	2.1
Material budget	4.3	0.8	0.1	6.2	0.4	
Hadronic interactions	1.9	0.9	0.1	1.4	0.7	
Total	9.8	8.3	12.1	9.5	7.3	9.0
Total (N_{ch} independent)	7.7	6.6	8.1	3	5	5
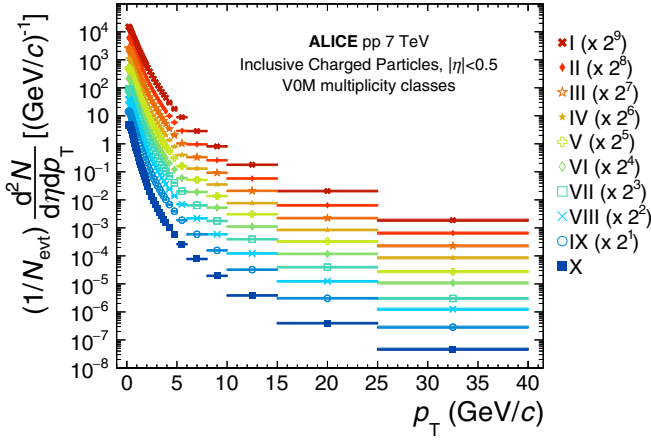
FIG. 4. Transverse momentum spectra of the sum of positively and negatively charged particles in different V0M event multiplicity classes.

and $\overline{\Omega}^+$ ($|y| < 0.5$). In the particular case of the ϕ, K^{*0}, and Ω^- measurements, some event classes were merged to allow for sufficient statistics. Particle and antiparticle as well as

charged and neutral kaon production rates are compatible within uncertainties.

Transverse momentum spectra are observed to become harder with increasing charged-particle multiplicity, with absolute changes in the spectrum shapes being more pronounced for particles with larger mass. The evolution of the p_T distributions with respect to the spectra in the INEL > 0 event class for the various particle species is shown in Fig. 6 and is observed to be identical for the two $\pi^\pm$ and K$^\pm$ mesons as well as for the p, Λ, Ξ^- baryons and their corresponding antiparticles. The spectra modification of ϕ and K^{*0} resonances follows the trend observed for baryons at $p_T < 2$ GeV/c while for larger momenta the modification is similar to the one observed for other mesons. Given that these mesonic resonances have a significantly higher mass than that of $\pi^\pm$ and K$^\pm$, this suggests that the spectra evolution with multiplicity is driven by the hadronic mass at low p_T and by the number of constituent quarks at higher p_T. It is also interesting to note that such behavior is not unique to high multiplicity but is present even for the lowest multiplicity class, where mass-dependent mechanisms such as radial flow are not expected to play a significant role.
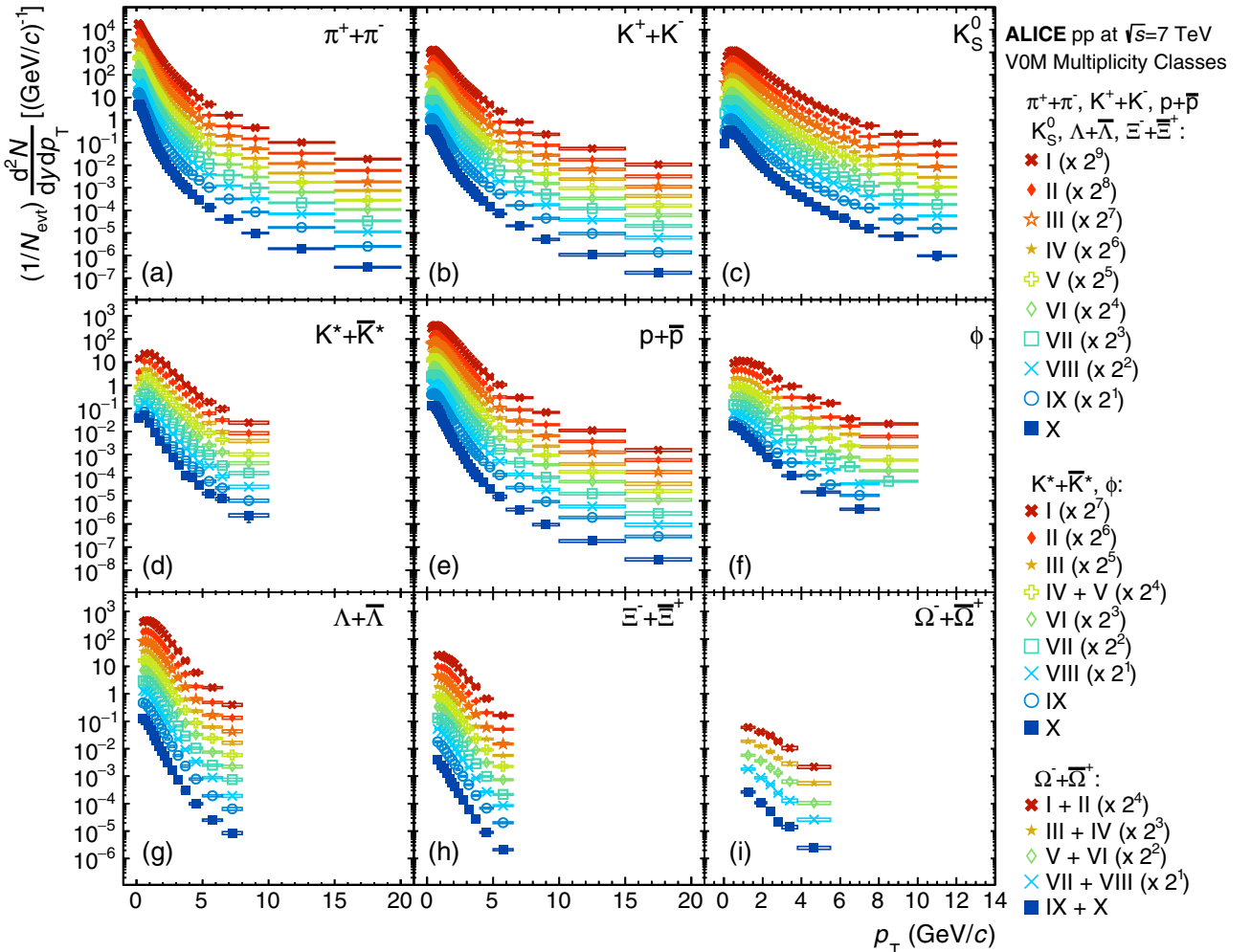
FIG. 5. Transverse momentum spectra of (a) $\pi^\pm$, (b) K$^\pm$, (c) K^0_S, (d) K^{*0}, (e) $p + \overline{p}$, (f) ϕ, (g) $\Lambda + \overline{\Lambda}$, (h) $\Xi^- + \overline{\Xi}^+$, and (i) $\Omega^- + \overline{\Omega}^+$. Top to bottom: high to low multiplicity; data are scaled by 2^n factors for better visibility.
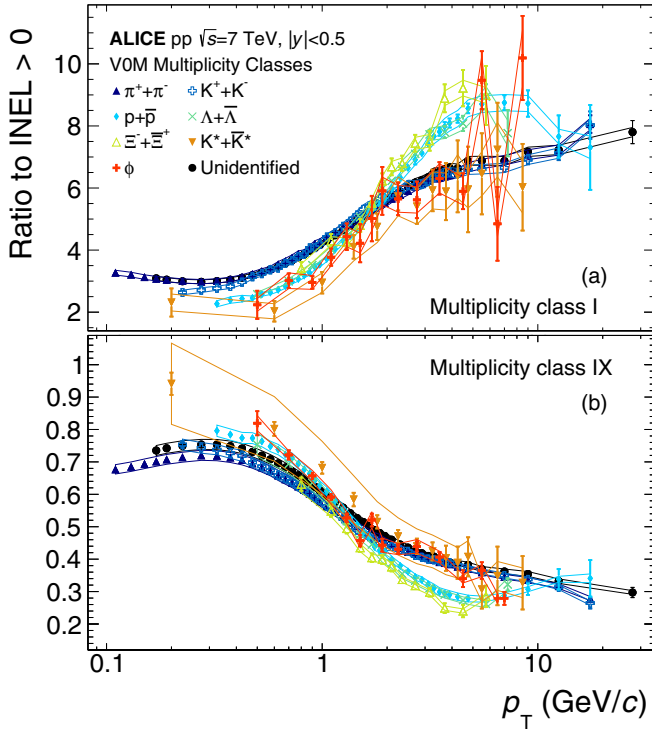
FIG. 6. Unidentified and identified particle spectra modification in (a) high-multiplicity and (b) low-multiplicity event classes. Statistical uncertainties are shown as errors bars and systematic uncertainties that are uncorrelated across multiplicities are shown as boxes. Other uncertainties are disregarded as they cancel in the ratio.

A comparison of the multiplicity dependence of the transverse momentum distributions can be performed by studying the ratios $p/\phi = (p + \overline{p})/\phi$, $K/\pi = (K^+ + K^-)/(\pi^+ + \pi^-)$, $p/\pi = (p + \overline{p})/(\pi^+ + \pi^-)$ and Λ/K^0_S as a function of p_T, as shown in Fig. 7 for the lowest and highest multiplicity classes in this work. Results are compared with measurements in p-Pb collisions at $\sqrt{s_{NN}} = 5.02$ TeV [4,6,43] as well as in Pb-Pb at $\sqrt{s_{NN}} = 2.76$ TeV [44,45]. The p/ϕ ratio is observed to decrease with p_T in pp and low-multiplicity p-Pb collisions but is seen to become progressively flatter for high-multiplicity p-Pb and Pb-Pb collisions. Given the similar mass of the particles involved in this ratio, it is possible that this flattening is a signature of significant radial flow in the larger systems. Furthermore, the baryon-to-meson ratios p/π and Λ/K^0_S exhibit a characteristic depletion at $p_T \sim 0.7$ GeV/c and an enhancement at intermediate p_T (~ 3 GeV/c), which is qualitatively similar to that observed in p-Pb and Pb-Pb collisions. Finally, the K/π ratio is observed to be relatively multiplicity independent, except for central Pb-Pb collisions, where a weak depletion (enhancement) at low (intermediate) p_T is visible.

While the observed changes in these particle ratios are quantitatively different in the various collision systems, it is worth noting that the final-state charged-particle multiplicities also cover very distinct ranges. If considered as a function of $dN_{ch}/d\eta$, the ratios measured in specific low-, mid-, and high-p_T intervals shown in Fig. 8 are seen to

depend on multiplicity in a remarkably similar manner for all collision systems, despite differences in energy and collision geometry.

B. Integrated yields and average momenta

The p_T-integrated yields dN/dy and mean transverse momenta $\langle p_T \rangle$ have been calculated using data in the measured momentum range and a Lévy-Tsallis parametrization to extrapolate the spectra down to zero p_T, similar to what was done in previous studies [22,39,40]. Several functional forms, such as Boltzmann, m_T-exponential, p_T-exponential, Fermi-Dirac, and Bose-Einstein functions, were used to estimate the systematic uncertainties associated to this procedure. For those functions that are unable to describe the p_T distributions in the full measured range, the fitting was restricted only to low p_T. The uncertainty on dN/dy and $\langle p_T \rangle$ associated to this procedure is shown in Table IX. The obtained dN/dy values for all multiplicity classes under study are summarized in Table XI for identified particles, while the $\langle p_T \rangle$ are reported in Tables X and XII for unidentified charged and identified particles, respectively.

The $\langle p_T \rangle$ values are observed to increase with multiplicity for all measured particle species, with the increase being more pronounced for heavier particles. This observation resembles that of previous measurements in p-Pb [4] and Pb-Pb [35] in which $\langle p_T \rangle$ values exhibit mass ordering for $\pi^\pm$, $K^\pm$, p, $\overline{p}$, Λ, $\overline{\Lambda}$, Ξ^-, $\overline{\Xi}^+$, Ω^-, and $\overline{\Omega}^+$. However, while in central Pb-Pb collisions particles with similar mass such as ϕ and p had similar $\langle p_T \rangle$ for central collisions, this is not the case for high-multiplicity pp events, where the $\langle p_T \rangle$ of the ϕ is significantly higher compared to that of the p, as can be seen in Fig. 9. This has also been observed in inelastic pp and in p-Pb [41] and is further indication that radial flow is the dominant mechanism determining spectra shapes only in very high multiplicity Pb-Pb. It is also interesting to note that at similar multiplicities $\langle p_T \rangle$ values for identified particles in pp and p-Pb are compatible within uncertainties despite differences in initial state and collision energy, pointing to a common mechanism at play in these two systems.

The multiplicity dependence of identified particle yields relative to pions is compared to p-Pb and Pb-Pb results in Fig. 10. Particles with a larger strangeness content are observed to be produced more abundantly with multiplicity, as can be seen in the Λ/π, Ξ/π, and Ω/π ratios [12]. The p/π ratio is observed to be constant within uncertainties except for the lowest multiplicity event class. This indicates that the increase of hyperon production with respect to pions is a phenomenon that does not originate from mass differences but is connected to strangeness content. Furthermore, the relative production of the ϕ increases with $dN_{ch}/d\eta$ by approximately 20%, similar to production of the Λ, a single-strange baryon. This suggests that ϕ production cannot be described solely by considering net strangeness or number of strange quark constituents. The K^{*0}/π ratio, on the other hand, exhibits a hint of a decrease with multiplicity. In nuclear collisions, this decrease is more pronounced and is typically considered a consequence of the rescattering of K^{*0} decay daughters during
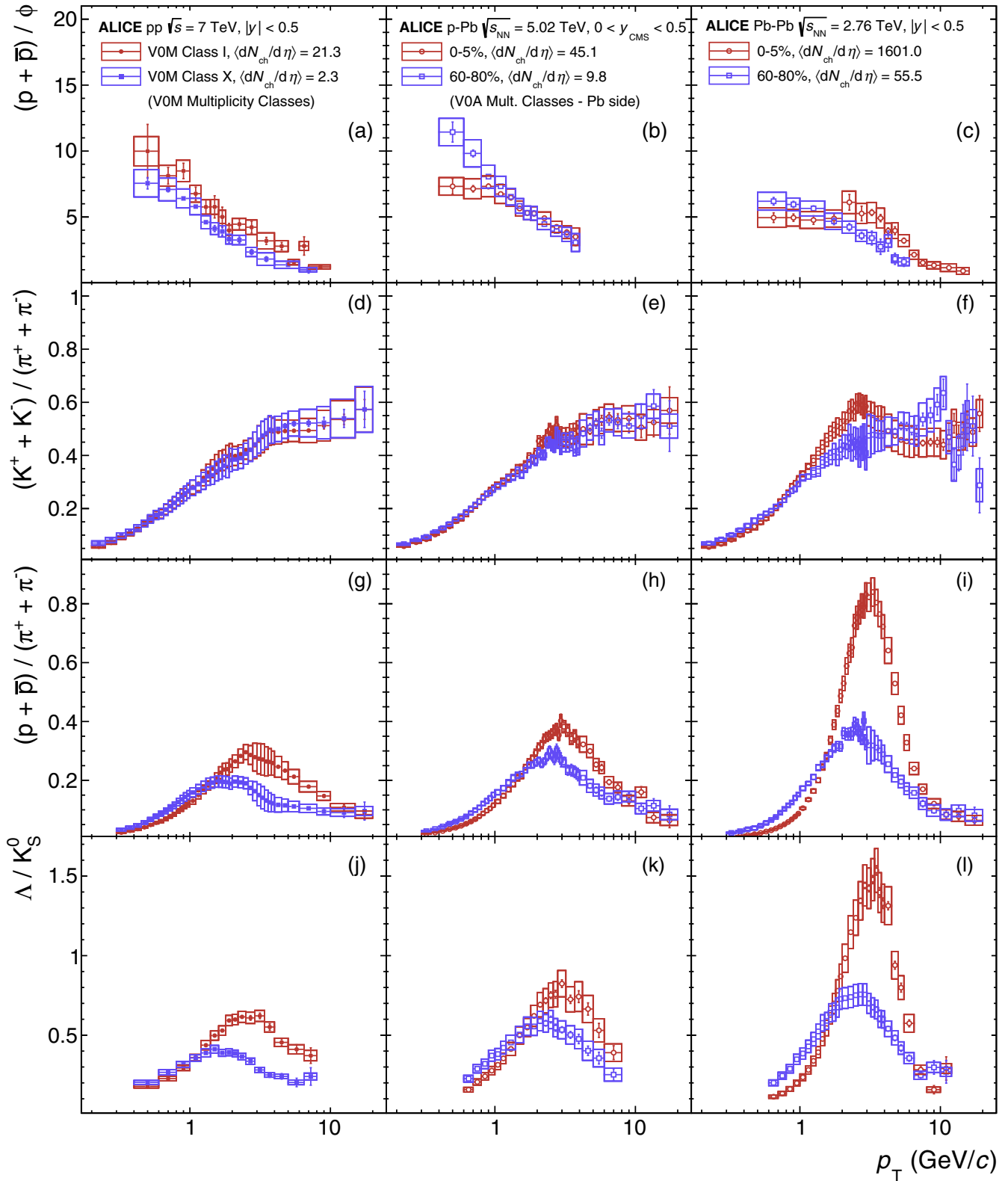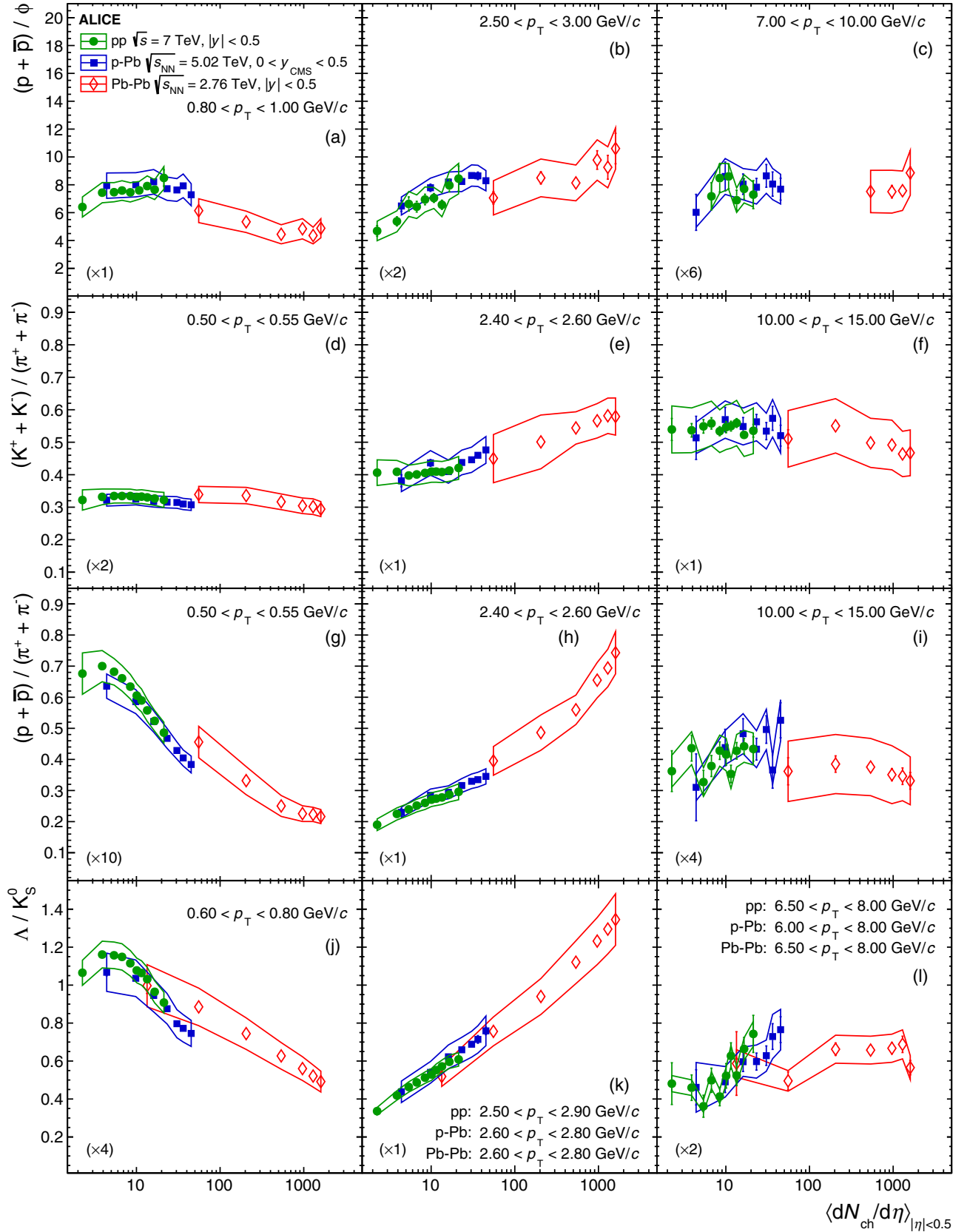
FIG. 7. Transverse momentum dependence of [(a)–(c)] $p/\phi = (p + \overline{p})/\phi$, [(d)–(f)] $K/\pi = (K^+ + K^-)/(\pi^+ + \pi^-)$, [(g)–(i)] $p/\pi = (p + \overline{p})/(\pi^+ + \pi^-)$, and [(j)–(l)] Λ/K_S^0 (from top to bottom row) yield ratios in [(a), (d), (g), (j)] pp, [(b), (e), (h), (k)] p-Pb, and [(c), (f), (i), (l)] Pb-Pb collisions for high- and low-multiplicity classes, respectively. Cancellation of common systematic uncertainties in the numerator and denominator was carried out only for the Λ/K_S^0, as in other cases the cancellation is nontrivial because of the use of various combined identification techniques or, in the case of resonances, of significantly different analysis strategy. Reference p-Pb and Pb-Pb data from Refs. [4,6,43–45].

FIG. 8. Transverse momentum dependence of [(a)–(c)] $p/\phi = (p + \overline{p})/\phi$, [(d)–(f)] $K/\pi = (K^+ + K^-)/(\pi^+ + \pi^-)$, [(g)–(i)] $p/\pi = (p + \overline{p})/(\pi^+ + \pi^-)$, and [(j)–(l)] Λ/K_S^0 yield ratios in [(a), (d), (g), (j)] low-, [(b), (e), (h), (k)] mid-, and [(c), (f), (i), (l)] high-p_T intervals in pp, p-Pb, and Pb-Pb collisions as a function of $\langle dN_{ch}/d\eta \rangle$. Reference p-Pb and Pb-Pb data are from Refs. [4,6,43–45].

TABLE IX. Overview of the systematic uncertainties associated to the low-p_T extrapolation used to calculate dN/dy and $\langle p_T \rangle$ for the various particle species. Values for the highest and the lowest multiplicity classes are given, with the smallest and highest uncertainties being associated to higher and lower multiplicity classes, respectively. If the dependence with multiplicity is negligible, only a single value is given.

Hadron species	Lowest	Fraction of extrapolated	Extrapolation uncertainty (%)	
	p_T (GeV/c)	dN/dy (%)	dN/dy	$\langle p_T \rangle$ (GeV/c)
$\pi^{\pm}$	0.1	9–10	1.5	1.5
$K^{\pm}$	0.2	6–14	0.5–2	0.5–2
$p\,(\overline{p})$	0.3	8–20	0.7–3	0.6–2.5
K_S^0	0.0	negl.	negl.	negl.
$\Lambda(\overline{\Lambda})$	0.4	10–25	2–6	2–4
$\Xi^-(\overline{\Xi}^+)$	0.6	16–36	3–10	2–7
$\Omega^-(\overline{\Omega}^+)$	0.9	27–47	4–13	2–8
ϕ	0.4	10–24	2–5	2–4
K^{*0}	0.0	negl.	negl.	negl.

a hadronic phase of the system evolution [5,46,47]. All these observations are consistent with previous measurements in p-Pb [4,6,41] and indicate that relative particle abundances can be described as a universal function of charged-particle density in pp and p-Pb collisions.

IV. DISCUSSION

A. Comparison to Monte Carlo models

The multiplicity dependence of the p_T-differential K/π, p/π, and Λ/K_S^0 ratios is compared to several Monte Carlo (MC) event generators; see Fig. 11. All predictions are obtained by performing selections on charged-particle multiplicities in the V0M acceptance and are compared to data parametrically as a function of $\langle dN_{ch}/d\eta \rangle$, as discussed in Sec. II A. The PYTHIA8 event generator in its Monash tune [8,30] is only successful in describing the qualitative features of the evolution of the baryon-to-meson ratios if color reconnection (CR) is allowed to occur, as observed already in previous work [48]. In contrast to the string-model-based PYTHIA, the HERWIG code implements hadronization in a clustering approach [49]. As shown in Fig. 11, the abilities of HERWIG7 to describe particle production at low and intermediate p_T are

TABLE X. Average transverse momenta ($|\eta| < 0.5$) for inclusive charged particles in different V0M event classes.

V0M	$\langle p_T \rangle$ (GeV/c)
I	$(6.969 \pm 0.001 \pm 0.183) \times 10^{-1}$
II	$(6.672 \pm 0.001 \pm 0.176) \times 10^{-1}$
III	$(6.442 \pm 0.001 \pm 0.171) \times 10^{-1}$
IV	$(6.275 \pm 0.001 \pm 0.167) \times 10^{-1}$
V	$(6.138 \pm 0.001 \pm 0.162) \times 10^{-1}$
VI	$(5.963 \pm 0.001 \pm 0.156) \times 10^{-1}$
VII	$(5.737 \pm 0.001 \pm 0.133) \times 10^{-1}$
VIII	$(5.527 \pm 0.001 \pm 0.106) \times 10^{-1}$
IX	$(5.214 \pm 0.001 \pm 0.103) \times 10^{-1}$
X	$(4.650 \pm 0.001 \pm 0.139) \times 10^{-1}$

still limited, but are currently being improved [50]. DIPSY, a model in which fragmenting strings are allowed to form color ropes which then hadronize with a higher effective string tension [51], is also able to reproduce the decreasing (increasing) trend of the baryon-to-meson ratios at low (high) p_T, but fails in describing the absolute values of these ratios. Furthermore, the EPOS-LHC event generator, which relies on parton-based Gribov-Regge theory and includes elements from hydrodynamics [9], predicts increased baryon-to-meson ratios at intermediate p_T as a consequence of radial flow, but overestimates the multiplicity dependence of these ratios and thus fails to quantitatively reproduce the measurements reported here. Finally, essentially all models are able to reproduce the fact that the K/π ratio is multiplicity independent, while not necessarily describing the absolute value well. These findings suggest that there is more than one physical mechanism that would lead to the dynamics observed in p_T-differential identified particle ratios, and a systematic study of other observables such as the flow coefficients v_n is required in order to discriminate among the various possibilities.

The p_T-integrated ratios are compared to predictions from the same Monte Carlo event generators in Fig. 12. The PYTHIA8 and HERWIG generators incorrectly predict no multiplicity dependence of relative strangeness production and therefore fail especially in the description of multistrange baryon production, while DIPSY and EPOS-LHC exhibit increased strangeness in high-multiplicity pp collisions but fail to predict a flat p/π ratio. None of the tested generators correctly reproduces the multiplicity dependence of the K^{*0}/π ratio, which is observed to decrease slightly. This comprehensive set of measurements provides essential input for all models aiming to describe flavor generation in pp collisions.

B. Comparison to blast-wave model predictions

The evolution of the p_T distribution with multiplicity in pp collisions is remarkably similar to the evolution observed in larger colliding systems, as underlined in Sec. III. In larger systems, this evolution can be interpreted as originating from

TABLE XI. Integrated particle yields $\frac{dN}{dy}|_{|y|<0.5}$ for various V0M multiplicity classes. The first error represents the statistical uncertainty and the second one is the systematic and extrapolation errors added in quadrature. See text for details.

V0M	$\frac{\pi^+ + \pi^-}{2}$	$\frac{K^+ + K^-}{2}$	$\frac{p + \overline{p}}{2}$
I	$10.035 \pm 0.007 \pm 0.519$	$1.374 \pm 0.003 \pm 0.093$	$(5.488 \pm 0.012 \pm 0.393) \times 10^{-1}$
II	$7.878 \pm 0.002 \pm 0.377$	$1.062 \pm 0.001 \pm 0.067$	$(4.369 \pm 0.005 \pm 0.301) \times 10^{-1}$
III	$6.459 \pm 0.001 \pm 0.306$	$(8.590 \pm 0.008 \pm 0.539) \times 10^{-1}$	$(3.599 \pm 0.004 \pm 0.246) \times 10^{-1}$
IV	$5.554 \pm 0.001 \pm 0.261$	$(7.308 \pm 0.006 \pm 0.453) \times 10^{-1}$	$(3.106 \pm 0.003 \pm 0.210) \times 10^{-1}$
V	$4.892 \pm 0.001 \pm 0.228$	$(6.388 \pm 0.006 \pm 0.394) \times 10^{-1}$	$(2.741 \pm 0.003 \pm 0.185) \times 10^{-1}$
VI	$4.138 \pm 0.001 \pm 0.192$	$(5.337 \pm 0.004 \pm 0.327) \times 10^{-1}$	$(2.316 \pm 0.002 \pm 0.156) \times 10^{-1}$
VII	$3.326 \pm 0.001 \pm 0.153$	$(4.231 \pm 0.003 \pm 0.258) \times 10^{-1}$	$(1.860 \pm 0.002 \pm 0.125) \times 10^{-1}$
VIII	$2.699 \pm 0.001 \pm 0.125$	$(3.383 \pm 0.003 \pm 0.207) \times 10^{-1}$	$(1.491 \pm 0.002 \pm 0.101) \times 10^{-1}$
IX	$(19.887 \pm 0.003 \pm 1.033) \times 10^{-1}$	$(2.429 \pm 0.002 \pm 0.162) \times 10^{-1}$	$(1.070 \pm 0.001 \pm 0.080) \times 10^{-1}$
X	$(12.100 \pm 0.002 \pm 0.857) \times 10^{-1}$	$(1.402 \pm 0.001 \pm 0.115) \times 10^{-1}$	$(5.856 \pm 0.005 \pm 0.532) \times 10^{-2}$

V0M	K_s^0	$\frac{\Lambda + \overline{\Lambda}}{2}$	$K^{*0} + \overline{K}^{*0}$
I	$1.337 \pm 0.004 \pm 0.069$	$(3.880 \pm 0.014 \pm 0.263) \times 10^{-1}$	$(3.478 \pm 0.185 \pm 0.404) \times 10^{-1}$
II	$1.040 \pm 0.002 \pm 0.053$	$(3.025 \pm 0.007 \pm 0.202) \times 10^{-1}$	$(2.730 \pm 0.078 \pm 0.328) \times 10^{-1}$
III	$(8.415 \pm 0.016 \pm 0.430) \times 10^{-1}$	$(2.445 \pm 0.006 \pm 0.165) \times 10^{-1}$	$(2.348 \pm 0.058 \pm 0.293) \times 10^{-1}$
IV	$(7.195 \pm 0.016 \pm 0.366) \times 10^{-1}$	$(2.076 \pm 0.005 \pm 0.140) \times 10^{-1}$	
V	$(6.300 \pm 0.015 \pm 0.320) \times 10^{-1}$	$(1.813 \pm 0.005 \pm 0.122) \times 10^{-1}$	$(1.950 \pm 0.045 \pm 0.230) \times 10^{-1}$
VI	$(5.296 \pm 0.010 \pm 0.268) \times 10^{-1}$	$(1.504 \pm 0.004 \pm 0.102) \times 10^{-1}$	$(1.568 \pm 0.027 \pm 0.197) \times 10^{-1}$
VII	$(4.237 \pm 0.009 \pm 0.214) \times 10^{-1}$	$(1.193 \pm 0.003 \pm 0.083) \times 10^{-1}$	$(1.313 \pm 0.033 \pm 0.157) \times 10^{-1}$
VIII	$(3.393 \pm 0.008 \pm 0.171) \times 10^{-1}$	$(9.361 \pm 0.028 \pm 0.616) \times 10^{-2}$	$(1.081 \pm 0.025 \pm 0.129) \times 10^{-1}$
IX	$(2.462 \pm 0.005 \pm 0.124) \times 10^{-1}$	$(6.450 \pm 0.017 \pm 0.461) \times 10^{-2}$	$(8.088 \pm 0.134 \pm 1.070) \times 10^{-2}$
X	$(1.391 \pm 0.003 \pm 0.069) \times 10^{-1}$	$(3.082 \pm 0.010 \pm 0.269) \times 10^{-2}$	$(5.105 \pm 0.073 \pm 0.741) \times 10^{-2}$

V0M	ϕ	$\frac{\Xi^- + \overline{\Xi}^+}{2}$	$\frac{\Omega^- + \overline{\Omega}^+}{2}$
I	$(1.697 \pm 0.051 \pm 0.172) \times 10^{-1}$	$(4.808 \pm 0.080 \pm 0.304) \times 10^{-2}$	$(4.137 \pm 0.132 \pm 0.389) \times 10^{-3}$
II	$(1.311 \pm 0.021 \pm 0.131) \times 10^{-1}$	$(3.584 \pm 0.037 \pm 0.231) \times 10^{-2}$	
III	$(1.098 \pm 0.017 \pm 0.114) \times 10^{-1}$	$(2.966 \pm 0.031 \pm 0.200) \times 10^{-2}$	$(2.541 \pm 0.098 \pm 0.262) \times 10^{-3}$
IV	$(8.711 \pm 0.104 \pm 0.874) \times 10^{-2}$	$(2.416 \pm 0.027 \pm 0.168) \times 10^{-2}$	
V		$(2.034 \pm 0.025 \pm 0.152) \times 10^{-2}$	$(1.488 \pm 0.048 \pm 0.149) \times 10^{-3}$
VI	$(6.536 \pm 0.088 \pm 0.673) \times 10^{-2}$	$(1.666 \pm 0.018 \pm 0.127) \times 10^{-2}$	
VII	$(5.178 \pm 0.076 \pm 0.536) \times 10^{-2}$	$(1.243 \pm 0.015 \pm 0.102) \times 10^{-2}$	$(9.313 \pm 0.589 \pm 1.186) \times 10^{-4}$
VIII	$(3.988 \pm 0.068 \pm 0.412) \times 10^{-2}$	$(9.443 \pm 0.142 \pm 0.849) \times 10^{-3}$	
IX	$(2.905 \pm 0.042 \pm 0.308) \times 10^{-2}$	$(6.023 \pm 0.087 \pm 0.638) \times 10^{-3}$	$(2.883 \pm 0.301 \pm 0.525) \times 10^{-4}$
X	$(1.729 \pm 0.029 \pm 0.221) \times 10^{-2}$	$(2.599 \pm 0.053 \pm 0.373) \times 10^{-3}$	

the hydrodynamical radial expansion of the produced medium [4,35] that can be studied by means of the Boltzmann-Gibbs blast-wave model (BG-BW) [52]. This model assumes a locally thermalized medium which expands with a common velocity field and then undergoes an instantaneous freeze-out phase. The average expansion velocity $\langle \beta_T \rangle$ and the kinematic freeze-out temperature T_{kin} can be extracted with a simultaneous fit to the p_T distribution of several particles for each multiplicity bin and the result can be used to predict the p_T spectra of particles with different masses.

The result of the simultaneous BG-BW fit to π, K, and p for the combined I+II V0M multiplicity class in pp collisions at $\sqrt{s} = 7$ TeV is shown as solid lines in Fig. 13 (top) for the p_T ranges 0.5–1, 0.2–1.5, and 0.3-3 GeV/c respectively. The predicted spectra for K_S^0, Λ, Ξ, Ω, K^{*0}, and ϕ are shown as dashed lines. The ratios between the data points and the fits or predictions are plotted in the bottom panels. Strange and multistrange hadron spectra are reasonably well predicted by

the BG-BW model in a p_T range which gets larger as the mass of the particle increases. This indicates that strange particles may follow a common motion together with lighter hadrons and suggests the presence of radial flow even in pp collisions. Resonances seem not to follow a similar expansion pattern, as there is no p_T region where the ratio of data/prediction is flat. This discrepancy between BG-BW predictions and resonance spectra extends to all multiplicity intervals studied.

The fit to pp spectra of π, K, and p has been performed for all the analyzed multiplicity bins and the values of $\langle \beta_T \rangle$ and T_{kin} are compared to those obtained for p-Pb and Pb-Pb collisions in Fig. 14. The fitting ranges are the same for all the three systems and a common color palette is used to highlight the average multiplicity corresponding to each point. Ellipses correspond to the 1-σ contour, estimated by fitting the p_T-differential spectra with total uncertainties, i.e., after adding statistical and systematic uncertainties in quadrature.

TABLE XII. Mean p_{T} (GeV/c) for various V0M multiplicity classes. The first error represents the statistical uncertainty and the second one is the systematic. See text for details.

V0M	$\frac{\pi^+ + \pi^-}{2}$	$\frac{K^+ + K^-}{2}$	$\frac{p + \bar{p}}{2}$
I	$(5.359 \pm 0.003 \pm 0.120) \times 10^{-1}$	$(9.332 \pm 0.009 \pm 0.142) \times 10^{-1}$	$1.135 \pm 0.001 \pm 0.022$
II	$(5.158 \pm 0.001 \pm 0.108) \times 10^{-1}$	$(8.892 \pm 0.004 \pm 0.127) \times 10^{-1}$	$1.071 \pm 0.001 \pm 0.021$
III	$(5.008 \pm 0.001 \pm 0.104) \times 10^{-1}$	$(8.558 \pm 0.004 \pm 0.135) \times 10^{-1}$	$1.020 \pm 0.001 \pm 0.021$
IV	$(4.898 \pm 0.001 \pm 0.100) \times 10^{-1}$	$(8.317 \pm 0.004 \pm 0.131) \times 10^{-1}$	$(9.815 \pm 0.007 \pm 0.197) \times 10^{-1}$
V	$(4.806 \pm 0.001 \pm 0.095) \times 10^{-1}$	$(8.113 \pm 0.004 \pm 0.133) \times 10^{-1}$	$(9.539 \pm 0.007 \pm 0.200) \times 10^{-1}$
VI	$(4.693 \pm 0.001 \pm 0.091) \times 10^{-1}$	$(7.867 \pm 0.003 \pm 0.130) \times 10^{-1}$	$(9.170 \pm 0.006 \pm 0.195) \times 10^{-1}$
VII	$(4.557 \pm 0.001 \pm 0.086) \times 10^{-1}$	$(7.538 \pm 0.003 \pm 0.133) \times 10^{-1}$	$(8.725 \pm 0.006 \pm 0.196) \times 10^{-1}$
VIII	$(4.427 \pm 0.001 \pm 0.082) \times 10^{-1}$	$(7.231 \pm 0.004 \pm 0.133) \times 10^{-1}$	$(8.285 \pm 0.006 \pm 0.192) \times 10^{-1}$
IX	$(4.237 \pm 0.001 \pm 0.081) \times 10^{-1}$	$(6.755 \pm 0.003 \pm 0.149) \times 10^{-1}$	$(7.716 \pm 0.005 \pm 0.222) \times 10^{-1}$
X	$(3.904 \pm 0.001 \pm 0.090) \times 10^{-1}$	$(5.885 \pm 0.003 \pm 0.159) \times 10^{-1}$	$(6.647 \pm 0.004 \pm 0.220) \times 10^{-1}$

V0M	K_s^0	$\frac{\Lambda + \bar{\Lambda}}{2}$	$K^{*0} + \overline{K}^{*0}$
I	$(9.367 \pm 0.025 \pm 0.119) \times 10^{-1}$	$1.277 \pm 0.003 \pm 0.028$	$1.307 \pm 0.038 \pm 0.043$
II	$(8.915 \pm 0.015 \pm 0.114) \times 10^{-1}$	$1.201 \pm 0.002 \pm 0.026$	$1.295 \pm 0.022 \pm 0.035$
III	$(8.612 \pm 0.014 \pm 0.108) \times 10^{-1}$	$1.144 \pm 0.002 \pm 0.026$	$1.211 \pm 0.018 \pm 0.037$
IV	$(8.350 \pm 0.014 \pm 0.104) \times 10^{-1}$	$1.103 \pm 0.002 \pm 0.025$	$1.150 \pm 0.016 \pm 0.035$
V	$(8.155 \pm 0.015 \pm 0.101) \times 10^{-1}$	$1.069 \pm 0.002 \pm 0.025$	
VI	$(7.900 \pm 0.011 \pm 0.098) \times 10^{-1}$	$1.027 \pm 0.001 \pm 0.025$	$1.064 \pm 0.011 \pm 0.033$
VII	$(7.563 \pm 0.014 \pm 0.094) \times 10^{-1}$	$(9.759 \pm 0.015 \pm 0.242) \times 10^{-1}$	$1.014 \pm 0.015 \pm 0.031$
VIII	$(7.299 \pm 0.014 \pm 0.089) \times 10^{-1}$	$(9.309 \pm 0.016 \pm 0.221) \times 10^{-1}$	$(9.557 \pm 0.135 \pm 0.292) \times 10^{-1}$
IX	$(6.869 \pm 0.012 \pm 0.082) \times 10^{-1}$	$(8.708 \pm 0.013 \pm 0.255) \times 10^{-1}$	$(8.656 \pm 0.088 \pm 0.283) \times 10^{-1}$
X	$(6.113 \pm 0.011 \pm 0.068) \times 10^{-1}$	$(7.669 \pm 0.014 \pm 0.319) \times 10^{-1}$	$(7.185 \pm 0.058 \pm 0.245) \times 10^{-1}$

V0M	ϕ	$\frac{\Xi^- + \overline{\Xi}^+}{2}$	$\frac{\Omega^- + \overline{\Omega}^+}{2}$
I	$1.440 \pm 0.023 \pm 0.037$	$1.463 \pm 0.012 \pm 0.036$	$1.645 \pm 0.025 \pm 0.056$
II	$1.360 \pm 0.012 \pm 0.034$	$1.382 \pm 0.007 \pm 0.035$	
III	$1.297 \pm 0.011 \pm 0.036$	$1.293 \pm 0.007 \pm 0.037$	
IV	$1.248 \pm 0.009 \pm 0.030$	$1.268 \pm 0.007 \pm 0.037$	$1.561 \pm 0.033 \pm 0.071$
V		$1.232 \pm 0.008 \pm 0.042$	
VI	$1.201 \pm 0.010 \pm 0.034$	$1.188 \pm 0.006 \pm 0.044$	$1.465 \pm 0.022 \pm 0.065$
VII	$1.127 \pm 0.010 \pm 0.033$	$1.141 \pm 0.007 \pm 0.048$	
VIII	$1.081 \pm 0.011 \pm 0.031$	$1.092 \pm 0.008 \pm 0.048$	$1.283 \pm 0.047 \pm 0.074$
IX	$(9.910 \pm 0.087 \pm 0.268) \times 10^{-1}$	$1.012 \pm 0.007 \pm 0.054$	
X	$(8.225 \pm 0.073 \pm 0.374) \times 10^{-1}$	$(8.975 \pm 0.095 \pm 0.634) \times 10^{-1}$	$1.125 \pm 0.061 \pm 0.101$
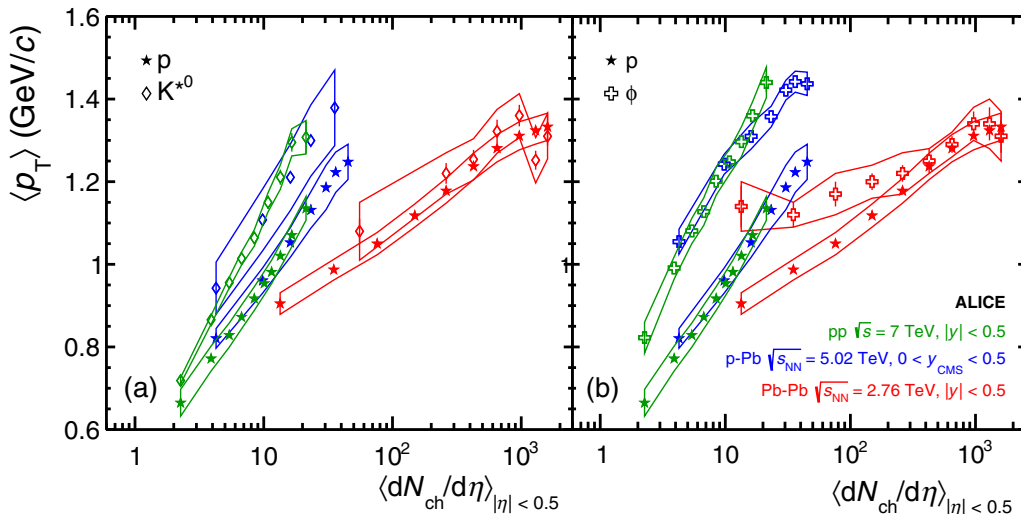
FIG. 9. Average transverse momentum (a) K^{*0} (left) and (b) ϕ compared to protons as a function of charged-particle multiplicity density.
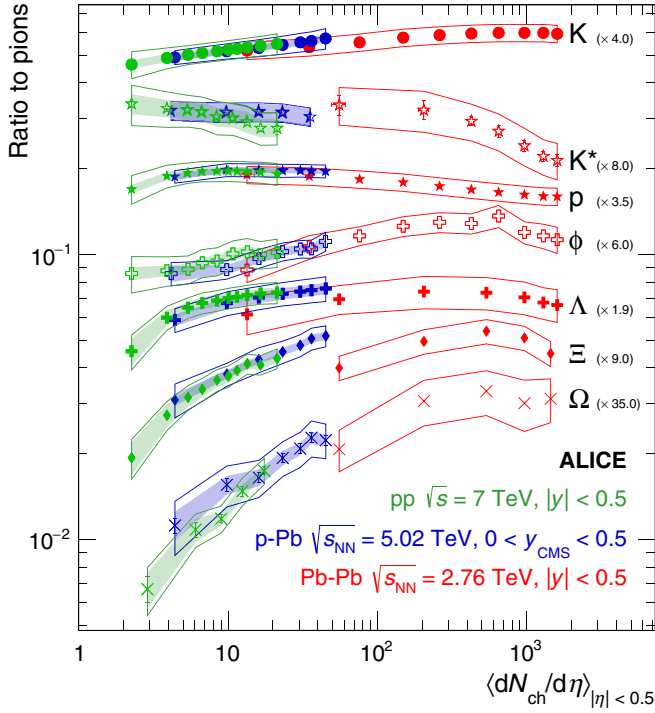
FIG. 10. Integrated particle-to-pion ratios as a function of $\langle dN_{\mathrm{ch}}/d\eta \rangle$ for pp, p-Pb, and Pb-Pb collisions. Reference p-Pb and Pb-Pb data are from Refs. [4,6,43–45].

Spectra in pp and p-Pb lead to very similar $\langle \beta_T \rangle$ and T_{kin} values when considering similar multiplicities, while in Pb-Pb at similar multiplicities, lower $\langle \beta_T \rangle$ are observed with respect to the other two systems. This behavior has been interpreted to be a consequence of stronger radial flow gradients in the smaller collision systems [53].

The CMS Collaboration has recently reported a similar study [54], where a BG-BW fit to the spectra of K_S^0 and Λ has been performed for the three colliding systems, selecting the multiplicity with a central rapidity estimator. The $\langle \beta_T \rangle$ -T_{kin} progression is found to be different for pp and p-Pb collisions at high multiplicity, but the numerous differences with respect to the analysis discussed here (multiplicity estimator, particles included, and treatment of systematic errors in the fits) do not allow for a quantitative comparison.

C. Comparison to statistical hadronization models

The measured abundances of hadrons produced in heavy-ion collisions have been successfully described by statistical hadronization models over a wide range of energies [55–57]. Statistical model calculations for central ultrarelativistic heavy-ion collisions are typically carried out in the grand-canonical ensemble. However, a grand-canonical description of particle production is only applicable if the volume $V = R^3$ of the system is sufficiently large and as a rule of thumb one needs $VT^3 > 1$ for a grand-canonical description to hold [58,59]. This condition must be fulfilled for each conserved charge separately. Several attempts were made to extend the picture of statistical hadronization to smaller systems such

as pp or even e^+e^- collisions [60–62]. While particle ratios of nonstrange particles are observed to be similar in small and large systems, the relative production of strange particles appears to be significantly lower in smaller systems. The data presented in Ref. [12] show for the first time that there is a continuous increase of strangeness production with increasing event multiplicity across various collision systems. In the strangeness canonical approach, it is assumed that the total amount of strange hadrons in the volume is small with respect to nonstrange hadrons. Thus the conservation of strangeness is guaranteed locally and not only globally while the bulk of the particles is still described in the grand-canonical ensemble. For further details on this approach, we refer, for instance, to Refs. [63–65]. The study presented here utilizes the implementation in the THERMUS 3.0 code [66]. Alternative implementations of the statistical model are for instance adopted in the codes of the GSI-Heidelberg [11,57] and SHARE [67] groups.

1. Correlation volume for strangeness production

Previous studies based on THERMUS were targeted to describe the evolution of multistrange particle production in p-Pb collisions as a function of event multiplicity [6]. In this case, the volume for particle production was chosen such that the charged pion multiplicity dN_π/dy at midrapidity corresponding to a window of $y = \pm 0.5$ units was correctly described by the model. This approach is equivalent to calculating strangeness suppression for a system whose total extension only corresponds to one unit of rapidity. Consequently, the model describes qualitatively the suppression pattern but overestimates the reduction of strangeness at small multiplicities. The discrepancy increases even further if this approach is extended to the smaller multiplicities which are covered in pp collisions.

In the study presented here, a similar approach as in Ref. [6] is followed: The strangeness saturation parameter is fixed to $\gamma_S = 1$, and the chemical potentials associated to baryon and electric charge quantum numbers are set to zero. The chemical freeze-out temperature T_{ch} is varied from 146 to 166 MeV as in Ref. [6], following recent results from lattice QCD calculations and their uncertainties [68] as well as by fits to experimental data from central Pb-Pb collisions [11,69]. Ratios of the production yields to pions are investigated for several particle species. In order to cancel the influence of the freeze-out temperature and to isolate the volume dependence, all ratios except for K^{*0} are normalized to the high-multiplicity limit, i.e., the grand-canonical saturation value for the model and the mean ratio in the 0–60% most central Pb-Pb collisions for the data. As the production rates of short-lived resonances in central heavy-ion collisions might be reduced by rescattering effects in the hadronic phase [5,41], the values for K^{0*} were normalized to the most peripheral bin in Pb-Pb collisions. The resulting double ratios are shown in Fig. 15.

In contrast to Ref. [6], the total volume V of the fireball was determined differently. While the strangeness conservation volume is also imposed to be of the size of the fireball ($V = V_C$), its absolute magnitude is not fixed to reproduce the pion multiplicity in a window of $y = \pm 0.5$ at midrapidity.
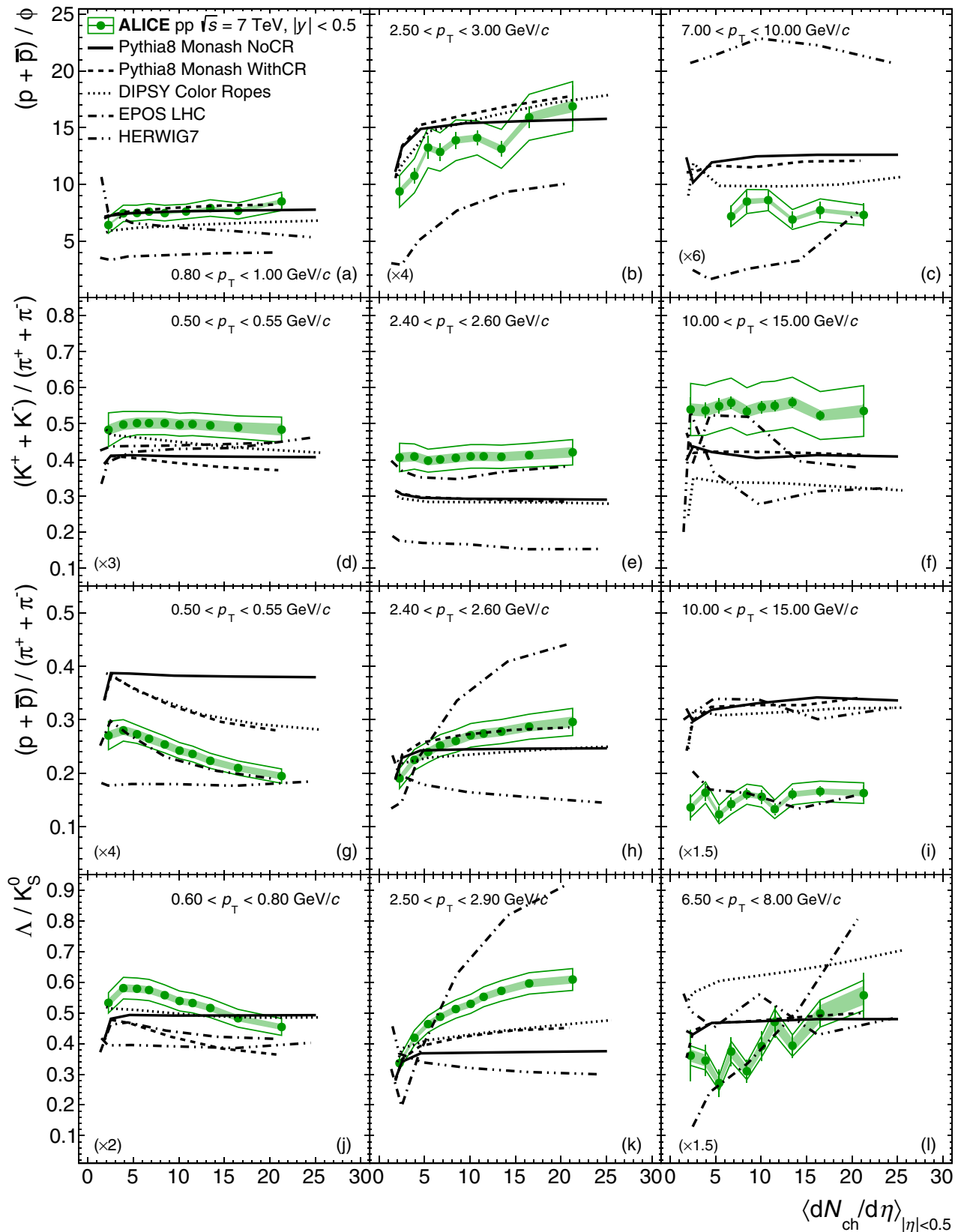
FIG. 11. Transverse momentum dependence of [(a)–(c)] $p/\phi = (p + \bar{p})/\phi$, [(d)–(f)] $K/\pi = (K^+ + K^-)/(\pi^+ + \pi^-)$, [(g)–(i)] $p/\pi = (p + \bar{p})/(\pi^+ + \pi^-)$, and [(j)–(l)] Λ/K_S^0 yield ratios in [(a), (d), (g), (j)] low-, [(b), (e), (h), (k)] mid-, and [(c), (f), (i), (l)] high-p_T intervals compared to several Monte Carlo event generators. Statistical uncertainties are shown as error bars, total systematic uncertainties are shown as hollow bands, and multiplicity-uncorrelated systematic uncertainties are shown as shaded bands.
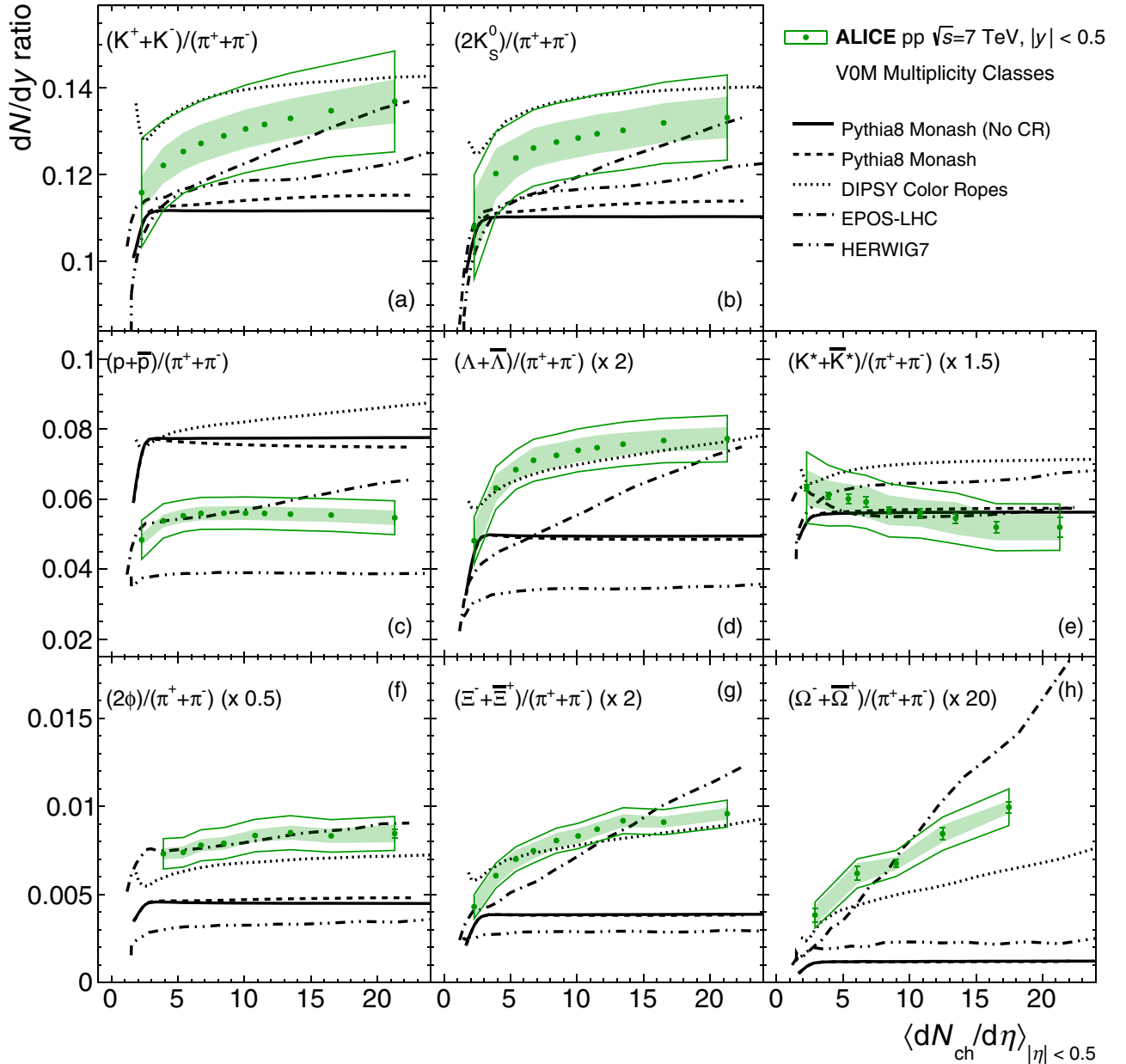
FIG. 12. Integrated yield ratios as a function of charged-particle multiplicity density compared to several Monte Carlo event generators. Statistical uncertainties are shown as error bars, total systematic uncertainties are shown as hollow bands, and multiplicity-uncorrelated systematic uncertainties are shown as shaded bands. For a complete description, please refer to the text.

Instead, it is fixed to reproduce a pion multiplicity which is larger by a factor k and thus corresponds to a larger rapidity window assuming a flat dependence of particle production as a function of rapidity. The same factor k was used for all particles and multiplicities. In practice, k corresponds to a constant scaling factor of dN_π/dy (the x axis in Fig. 15), and this feature is used for its numerical determination: The exact value of k was optimized in a one-parameter fit of the functions describing the evolution of the double ratios versus dN_π/dy to the experimental data. For the determination of the systematic uncertainty on the value of k, an alternative normalization scheme for the data was applied (normalization to

the highest available centrality bin) and the procedure for the determination of k was repeated. A value of $k = 1.35 \pm 0.28$ is obtained corresponding to a rapidity window of $y = \pm 0.67$. The results thus indicate that the total correlation volume for strangeness production extends over about 1.35 units in rapidity. In other words, strangeness as a conserved quantity in QCD can be effectively equilibrated over this distance in the system. Similar values can be obtained from purely theoretical considerations on causality constraints [70]. Furthermore, the size of the correlation window is also compatible with similar estimates for charm production [71,72]. We also note that this value is smaller than the plateau in the rapidity distribution
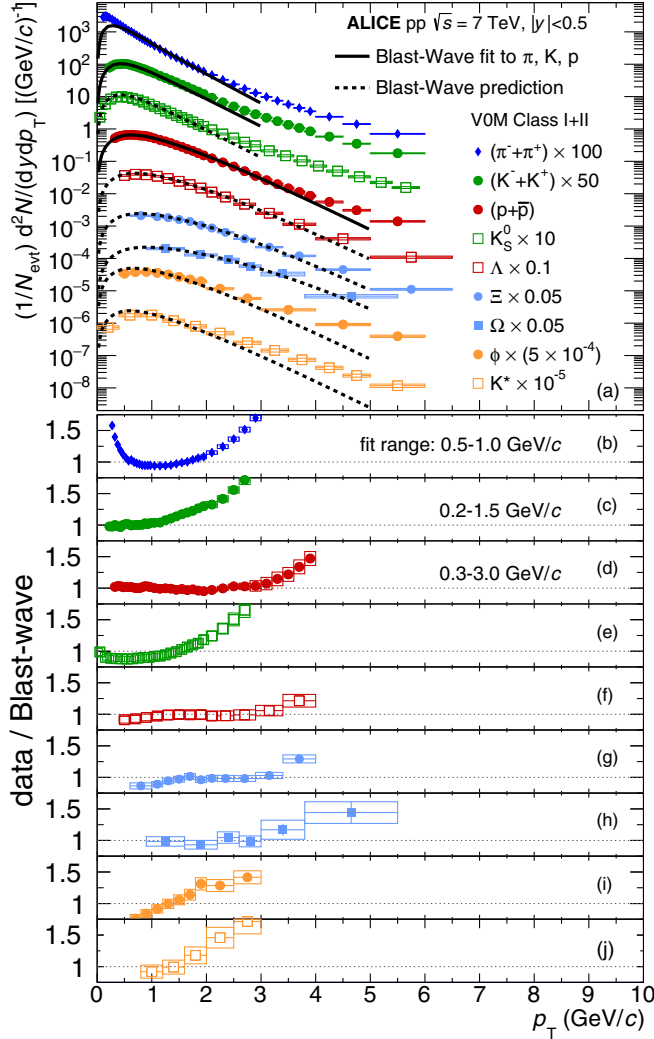
FIG. 13. (a) Simultaneous BG-BW fit to π, K, and p spectra from high-multiplicity (I+II V0M classes) pp collisions. Solid lines correspond to the fit, and dashed lines to the prediction. [(b)–(j)] Ratio data/fit(prediction) for the various particle species.

at LHC energies which extends typically over three to four units [73,74] and is thus meaningful from a physical point of view.

2. Comparison to experimental data

As shown in Fig. 15, this approach allows for a qualitative description of particle ratios as a function of event multiplicity. They can be naturally described within the framework of strangeness canonical suppression. The deviations observed for the K^{*0} meson in central Pb-Pb collisions can be ascribed to the aforementioned rescattering effects in the hadronic phase [75]. Furthermore, differences between the model and the data in the most peripheral Pb-Pb collisions in case of Ω and Ξ can be potentially reduced with core-corona corrections [76].

From a quantitative point of view, essentially all data points can be described within 1–2 standard deviations. A potentially different trend is only observed for the ϕ-meson
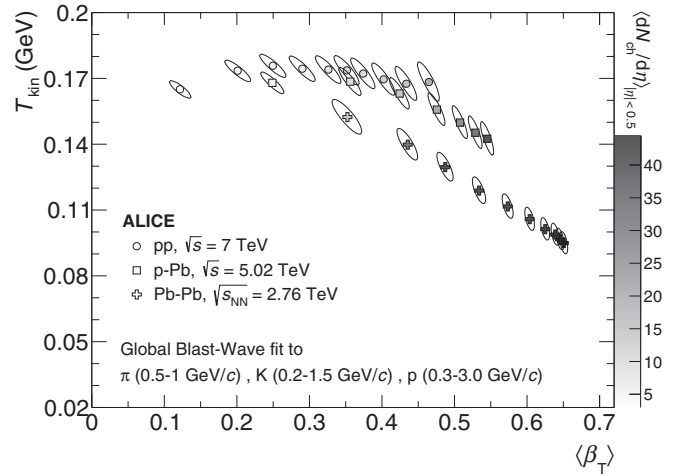
FIG. 14. Kinematic freeze-out temperature parameter T_{kin} vs average expansion velocity $\langle \beta_T \rangle$ from a simultaneous BG-BW fit to π, K, and p spectra measured in pp, p-Pb, and Pb-Pb collisions. The shade of the data points indicates the corresponding average charged-particle multiplicity density.

for which—as a strangeness-neutral particle—a flat dependence as a function of event multiplicity is expected from the model, but which shows a rising and falling trend in data. Future experimental data will be needed in order to clarify the significance of this deviation. It must be noted, though, that the ϕ meson also deviates from a common blast-wave fit to other light-flavor hadrons in peripheral Pb-Pb collisions, indicating an out-of-equilibrium production except for most central Pb-Pb collisions [5].

Independently of the experimental precision and possible higher order effects in the particle production mechanisms, we find that the strangeness canonical approach can reproduce the multiplicity dependence of all measured light-flavor hadrons across various collision systems to within 10–20%.

V. SUMMARY AND CONCLUSIONS

A comprehensive set of unidentified and identified p_{T}-differential particle spectra at midrapidity has been measured in pp collisions at $\sqrt{s} = 7$ TeV as a function of charged-particle multiplicity, complementing the existing measurements in p-Pb and Pb-Pb collisions and allowing for a comparison of these different collision systems. In pp collisions, all transverse momentum spectra are observed to become harder with progressively larger charged-particle multiplicity density, with the effect being more pronounced for heavier particles. In addition, the modification of spectra with respect to the inclusive measurement follows a different pattern for mesons and baryons, except for resonances, which follow baryons at a low p_{T} of up to approximately 2 GeV/c and tend to be modified similarly to mesons above a p_{T} of 2 GeV/c. Furthermore, it has been demonstrated that the evolution of the baryon/meson ratios as a function of $\langle dN_{\text{ch}}/d\eta \rangle$ exhibits a universal pattern for all collision systems. This behavior might indicate a common mechanism at work that depends
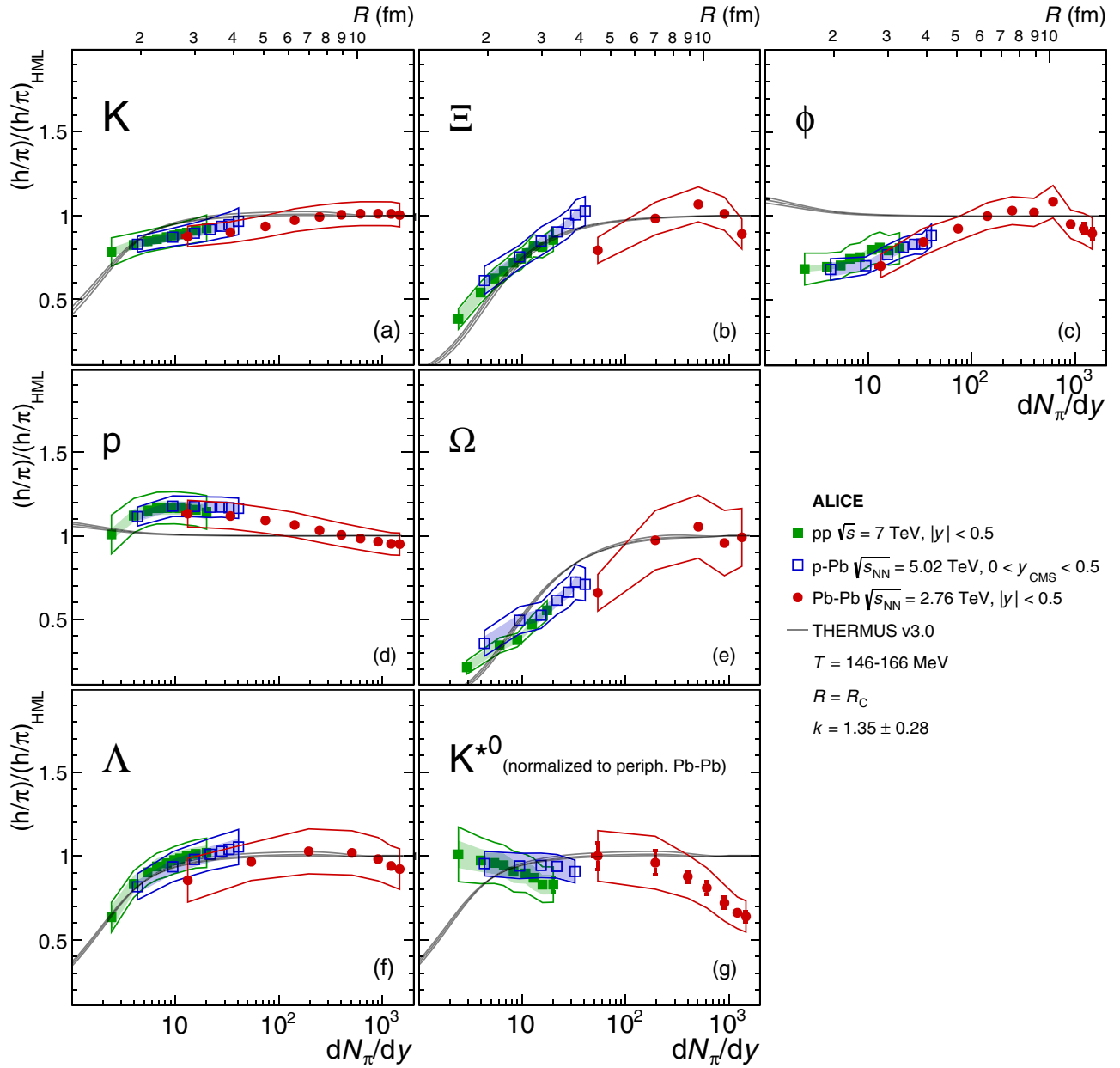
FIG. 15. Ratios of the production yields to pions for several particle species as a function of the midrapidity pion yields for *pp*, *p*-Pb, and Pb-Pb colliding systems compared to the THERMUS model prediction for the strangeness canonical suppression (continuous curves), in which only the system size is varied. All values except for the K^{*0} are normalized to the high multiplicity limit (see text for details). The upper axis shows the radius R of the correlation volume $V = R^3$ which corresponds to the predicted particle ratios. The variations in model prediction curves correspond to variations of the chemical freeze-out temperature at 146, 156, and 166 MeV. Reference *p*-Pb and Pb-Pb data are from Refs. [4,6,43–45].

solely on final-state multiplicity density. A similar statement can also be made for integrated particle ratios, which are observed to depend on $\langle dN_{ch}/d\eta \rangle$ in approximately the same way for any colliding system despite crucial differences in the initial states as well as colliding energies. The simplest interpretation of this similarity is that in both cases the final state is a thermalized system whose volume at hadronization is proportional to the charged-particle multiplicity density.

In order to test the assertion of equilibration more quantitatively, the blast-wave model was employed to check if the hypothesis of kinematic equilibrium can describe p_T-differential particle spectra at low momenta, and a statistical hadronization model employing a strangeness-canonical approach was used to check for chemical equilibrium. In all cases, all particle species except for resonances are described within 10–20% by these models. It is also interesting to note that, within the statistical hadronization model employed

here, the correlation volume over which strangeness production is equilibrated extends over approximately 1.35 units of rapidity.

The results are also compared to predictions from event generators, which are only able to describe the evolution of p_{T}-differential particle spectra with $\langle dN_{\mathrm{ch}}/d\eta \rangle$ if mechanisms such as color reconnection, color ropes, or radial flow, as is the case for PYTHIA, DIPSY, and EPOS-LHC, respectively, were present. To distinguish between these different mechanisms requires more studies, both experimental and theoretical.

The multiplicity dependence of relative abundances of identified particles was also compared to several event generators and it was found that no generator is able to fully describe the whole observed dynamics satisfactorily. This comprehensive set of results therefore provides a challenge to the theory community and represents an opportunity to study not only pp collisions specifically, but also hadronization at high energies in general.

[1] B. Abelev *et al.* (ALICE Collaboration), Long-range angular correlations on the near and away side in *p*-Pb collisions at $\sqrt{s_{NN}} = 5.02$ TeV, Phys. Lett. B **719**, 29 (2013).

[2] V. Khachatryan *et al.* (CMS Collaboration), Evidence for Collective Multiparticle Correlations in *p*-Pb Collisions, Phys. Rev. Lett. **115**, 012301 (2015).

[3] B. Abelev *et al.* (ALICE Collaboration), Long-range angular correlations of π, K, and p in p-Pb collisions at $\sqrt{s_{NN}} = 5.02$ TeV, Phys. Lett. B **726**, 164 (2013).

[4] B. Abelev *et al.* (ALICE Collaboration), Multiplicity dependence of pion, kaon, proton, and lambda production in p-Pb collisions at $\sqrt{s_{NN}} = 5.02$ TeV, Phys. Lett. B **728**, 25 (2014).

[5] B. Abelev *et al.* (ALICE Collaboration), $K^*(892)^0$ and $\phi(1020)$ production in Pb-Pb collisions at $\sqrt{s_{NN}} = 2.76$ TeV, Phys. Rev. C **91**, 024609 (2015).

[6] J. Adam *et al.* (ALICE Collaboration), Multi-strange baryon production in p–Pb collisions at $\sqrt{s_{NN}} = 5.02$ TeV, Phys. Lett. B **758**, 389 (2015).

[7] G. Aad *et al.* (ATLAS Collaboration), Observation of Long-Range Elliptic Azimuthal Anisotropies in $\sqrt{s} = 13$ and 2.76 TeV pp Collisions with the ATLAS Detector, Phys. Rev. Lett. **116**, 172301 (2016).

[8] P. Z. Skands, S. Carrazza, and J. Rojo, Tuning PYTHIA 8.1:The Monash 2013 Tune, Eur. Phys. J. C **74**, 3024 (2014).

[9] T. Pierog, I. Karpenko, J. M. Katzy, E. Yatsenko, and K. Werner, EPOS LHC: Test of collective hadronization with data measured at the CERN Large Hadron Collider, Phys. Rev. C **92**, 034906 (2015).

[10] R. Derradi de Souza, T. Koide, and T. Kodama, Hydrodynamic approaches in relativistic heavy ion reactions, Prog. Part. Nucl. Phys. **86**, 35 (2016).

[11] A. Andronic, P. Braun-Munzinger, K. Redlich, and J. Stachel, Decoding the phase structure of QCD via particle production at high energy, Nature **561**, 321 (2018).

[12] J. Adam *et al.* (ALICE Collaboration), Enhanced production of multi-strange hadrons in high-multiplicity proton-proton collisions, Nat. Phys. **13**, 535 (2017).

[13] K. Aamodt *et al.* (ALICE Collaboration), The ALICE experiment at the CERN LHC, JINST **3**, S08002 (2008).

[14] B. Abelev *et al.* (ALICE Collaboration), Performance of the ALICE Experiment at the CERN LHC, Int. J. Mod. Phys. A **29**, 1430044 (2014).

[15] G. Dellacasa *et al.* (ALICE Collaboration), ALICE technical design report of the inner tracking system (ITS), Report No. CERN-LHCC-99-12, Geneva (1999).

[16] K. Aamodt *et al.* (ALICE Collaboration), Alignment of the ALICE Inner Tracking System with cosmic-ray tracks, JINST **5**, P03003 (2010).

[17] J. Alme *et al.* (ALICE Collaboration), The ALICE TPC, a large three-dimensional tracking device with fast readout for ultra-high multiplicity events, Nucl. Instrum. Methods A **622**, 316 (2010).

[18] ALICE Collaboration, Performance of the ALICE time-of-flight detector at the LHC, Eur. Phys. J. Plus **128**, 44 (2013).

[19] E. Abbas *et al.* (ALICE Collaboration), Performance of the ALICE VZERO system, J. Instrument. **8**, P10016 (2013).

[20] J. Adam *et al.* (ALICE Collaboration), Determination of the event collision time with the ALICE detector at the LHC, Eur. Phys. J. Plus **132**, 99 (2017).

[21] ALICE Collaboration, The ALICE definition of primary particles, 2017, ALICE-PUBLIC-2017-005, https://cds.cern.ch/record/2270008

[22] J. Adam *et al.* (ALICE Collaboration), Measurement of pion, kaon, and proton production in proton-proton collisions at $\sqrt{s} = 7$ TeV, Eur. Phys. J. C **75**, 226 (2015).

[23] T. Sjöstrand, S. Mrenna, and P. Z. Skands, PYTHIA6.4 physics and manual, JHEP 05 (2006) 026.

[24] P. Z. Skands, Tuning Monte Carlo generators: The Perugia Tunes, Phys. Rev. D **82**, 074018 (2010).

[25] R. Brun, F. Bruyant, F. Carminati, S. Giani, M. Maire, A. McPherson, G. Patrick, and L. Urban, GEANT: Detector description and simulation tool, Report No. CERN-W-5013, Geneva (1994).

[26] B. Abelev *et al.* (ALICE Collaboration), Pseudorapidity Density of Charged Particles in $p + $ Pb Collisions at $\sqrt{s_{NN}} = 5.02$ TeV, Phys. Rev. Lett. **110**, 032301 (2013).

[27] J. Adam *et al.* (ALICE Collaboration), Pseudorapidity and transverse-momentum distributions of charged particles in proton-proton collisions at $\sqrt{s} = 13$ TeV, Phys. Lett. B **753**, 319 (2016).

[28] B. Abelev *et al.* (ALICE Collaboration), J/ψ production as a function of charged particle multiplicity in pp collisions at $\sqrt{s} = 7$ TeV, Phys. Lett. B **712**, 165 (2012).

[29] B. Abelev *et al.* (ALICE Collaboration), Multiplicity dependence of the average transverse momentum in pp, p-Pb, and Pb-Pb collisions at the LHC, Phys. Lett. B **727**, 371 (2013).

[30] T. Sjöstrand, S. Mrenna, and P. Z. Skands, A brief introduction to PYTHIA 8.1, Comput. Phys. Commun. **178**, 852 (2008).

[31] J. Adam *et al.* (ALICE Collaboration), Centrality dependence of particle production in p-Pb collisions at $\sqrt{s_{NN}} = 5.02$ TeV, Phys. Rev. C **91**, 064905 (2015).

[32] A. Ferrari, P. R. Sala, A. Fasso, and J. Ranft, FLUKA: A multi-particle transport code (Program version 2005), Report No. CERN-2005-010, Geneva (2005).

[33] T. Böhlen, F. Cerutti, M. Chin, A. Fassò, A. Ferrari, P. Ortega, A. Mairani, P. Sala, G. Smirnov, and V. Vlachoudis, The FLUKA code: Developments and challenges for high energy and medical applications, Nucl. Data Sheets **120**, 211 (2014).

[34] B. Abelev *et al.* (ALICE Collaboration), Energy dependence of the transverse momentum distributions of charged particles in pp collisions measured by ALICE, Eur. Phys. J. C **73**, 2662 (2013).

[35] B. Abelev *et al.* (ALICE Collaboration), Centrality dependence of π, K, p production in Pb-Pb collisions at $\sqrt{s_{NN}} = 2.76$ TeV, Phys. Rev. C **88**, 044910 (2013).

[36] J. Adam *et al.* (ALICE Collaboration), Particle identification in ALICE: A Bayesian approach, Eur. Phys. J. Plus **131**, 168 (2016).

[37] E. Abbas *et al.* (ALICE Collaboration), Mid-rapidity anti-baryon to baryon ratios in pp collisions at $\sqrt{s} = 0.9$, 2.76 and 7 TeV measured by ALICE, Eur. Phys. J. C **73**, 2496 (2013).

[38] C. Patrignani *et al.* (Particle Data Group Collaboration), Review of particle physics, Chin. Phys. C **40**, 100001 (2016).

[39] B. Abelev *et al.* (ALICE Collaboration), Multi-strange baryon production in pp collisions at $\sqrt{s} = 7$ TeV with ALICE, Phys. Lett. B **712**, 309 (2012).

[40] B. Abelev *et al.* (ALICE Collaboration), Production of $K^*(892)^0$ and $\phi(1020)$ in pp collisions at $\sqrt{s} = 7$ TeV, Eur. Phys. J. C **72**, 2183 (2012).

[41] J. Adam *et al.* (ALICE Collaboration), Production of K* $(892)^0$ and ϕ (1020) in p-Pb collisions at $\sqrt{s_{NN}} = 5.02$ TeV, Eur. Phys. J. C **76**, 245 (2016).

[42] S. Acharya *et al.* (ALICE Collaboration), Transverse momentum spectra and nuclear modification factors of charged particles in pp, p-Pb, and Pb-Pb collisions at the LHC, J. High Energy Phys. 11 (2018) 013.

[43] J. Adam *et al.* (ALICE Collaboration), Multiplicity dependence of charged pion, kaon, and (anti)proton production at large

transverse momentum in p-Pb collisions at $\sqrt{s_{NN}} = 5.02$ TeV, Phys. Lett. B **760**, 720 (2016).

[44] B. Abelev *et al.* (ALICE Collaboration), K_S^0 and Λ Production in Pb-Pb Collisions at $\sqrt{s_{NN}} = 2.76$ TeV, Phys. Rev. Lett. **111**, 222301 (2013).

[45] B. Abelev *et al.* (ALICE Collaboration), Production of charged pions, kaons, and protons at large transverse momenta in pp and Pb-Pb collisions at $\sqrt{s_{NN}} = 2.76$ TeV, Phys. Lett. B **736**, 196 (2014).

[46] M. Bleicher and H. Stoecker, Dynamics and freeze-out of hadron resonances at RHIC, J. Phys. G **30**, S111 (2004).

[47] C. Markert, G. Torrieri, and J. Rafelski, *Strange hadron resonances: Freeze-out probes in heavy-ion collisions*, AIP Conf. Proc. No. 631 (AIP, New York, 2002), 533.

[48] A. Ortiz Velasquez, P. Christiansen, E. Cuautle Flores, I. A. Maldonado Cervantes, and G. Paić, Color Reconnection and Flow-Like Patterns in pp Collisions, Phys. Rev. Lett. **111**, 042001 (2013).

[49] M. Bahr *et al.*, HERWIG++ physics and manual, Eur. Phys. J. C **58**, 639 (2008).

[50] S. Gieseke, F. Loshaj, and P. Kirchgaeßer, Soft and diffractive scattering with the cluster model in HERWIG, Eur. Phys. J. C **77**, 156 (2017).

[51] C. Bierlich, G. Gustafson, L. Lönnblad, and A. Tarasov, Effects of overlapping strings in pp collisions, JHEP 03 (2015) 148.

[52] E. Schnedermann, J. Sollfrank, and U. Heinz, Thermal phenomenology of hadrons from 200 A GeV S+S collisions, Phys. Rev. C **48**, 2462 (1993).

[53] E. Shuryak and I. Zahed, High-multiplicity pp and pA collisions: Hydrodynamics at its edge, Phys. Rev. C **88**, 044915 (2013).

[54] CMS Collaboration, Multiplicity and rapidity dependence of strange hadron production in pp, p-Pb, and Pb-Pb collisions at the LHC, Phys. Lett. B **768**, 103 (2017).

[55] A. Andronic, P. Braun-Munzinger, K. Redlich, and J. Stachel, The thermal model on the verge of the ultimate test: Particle production in Pb-Pb collisions at the LHC, J. Phys. G **38**, 124081 (2011).

[56] J. Cleymans and K. Redlich, Unified Description of Freezeout Parameters in Relativistic Heavy Ion Collisions, Phys. Rev. Lett. **81**, 5284 (1998).

[57] A. Andronic, P. Braun-Munzinger, and J. Stachel, Hadron production in central nucleus nucleus collisions at chemical freeze-out, Nucl. Phys. A **772**, 167 (2006).

[58] R. Hagedorn and K. Redlich, Statistical thermodynamics in relativistic particle and ion physics: Canonical or grand canonical? Z. Phys. C **27**, 541 (1985).

[59] J. Rafelski and M. Danos, The importance of the reaction volume in hadronic collisions, Phys. Lett. B **97**, 279 (1980).

[60] K. Redlich, A. Andronic, F. Beutler, P. Braun-Munzinger, and J. Stachel, Canonical statistical model and hadron production in $e + e-$ annihilations, J. Phys. G **36**, 064021 (2009).

[61] F. Becattini, Universality of thermal hadron production in pp, p anti-p, and $e + e-$ collisions, in *Universality Features in Multihadron Production and the Leading Effect: Proceedings, 33rd Workshop of the INFN Eloisatron Project, Erice, Italy, October 19–25, 1996* (1996), pp. 74–104, DFF-263-12-1996; arXiv:hep-ph/9701275 [hep-ph].

[62] I. Kraus, J. Cleymans, H. Oeschler, and K. Redlich, Particle production in p-p collisions and prediction for LHC energy, Phys. Rev. C **79**, 014901 (2009).

[63] P. Braun-Munzinger, K. Redlich, and J. Stachel, Particle production in heavy ion collisions, Quark-Gluon Plasma **3**, 491 (2004).

[64] S. Hamieh, K. Redlich, and A. Tounsi, Canonical description of strangeness enhancement from p-A to Pb Pb collisions, Phys. Lett. B **486**, 61 (2000).

[65] J. Cleymans, A. Forster, H. Oeschler, K. Redlich, and F. Uhlig, On the chemical equilibration of strangeness-exchange reaction in heavy-ion collisions, Phys. Lett. B **603**, 146 (2004).

[66] S. Wheaton and J. Cleymans, THERMUS: A thermal model package for ROOT, Comput. Phys. Commun. **180**, 84 (2009).

[67] M. Petran, J. Letessier, J. Rafelski, and G. Torrieri, SHARE with CHARM, Comput. Phys. Commun. **185**, 2056 (2014).

[68] A. Bazavov *et al.* (HotQCD Collaboration), Equation of state in (2+1)-flavor QCD, Phys. Rev. D **90**, 094503 (2014).

[69] S. Acharya *et al.* (ALICE Collaboration), Production of ^{4}He and $^4\overline{\text{He}}$ in Pb-Pb collisions at $\sqrt{s_{NN}} = 2.76$ TeV at the LHC, Nucl. Phys. A **971**, 1 (2018).

[70] P. Castorina and H. Satz, Causality constraints on hadron production in high energy collisions, Int. J. Mod. Phys. E **23**, 1450019 (2014).

[71] A. Andronic, P. Braun-Munzinger, K. Redlich, and J. Stachel, Statistical hadronization of charm in heavy ion collisions at SPS, RHIC, and LHC, Phys. Lett. B **571**, 36 (2003).

[72] A. Andronic, P. Braun-Munzinger, K. Redlich, and J. Stachel, Statistical hadronization of heavy quarks in ultra-relativistic nucleus-nucleus collisions, Nucl. Phys. A **789**, 334 (2007).

[73] J. Adam *et al.*, Charged-particle multiplicities in proton–proton collisions at $\sqrt{s} = 0.9$ to 8 TeV, Eur. Phys. J. C **77**, 33 (2017).

[74] E. Abbas *et al.* (ALICE Collaboration), Centrality dependence of the pseudorapidity density distribution for charged particles in Pb-Pb collisions at $\sqrt{s_{NN}} = 2.76$ TeV, Phys. Lett. B **726**, 610 (2013).

[75] A. G. Knospe, C. Markert, K. Werner, J. Steinheimer, and M. Bleicher, Hadronic resonance production and interaction in partonic and hadronic matter in the EPOS3 model with and without the hadronic afterburner UrQMD, Phys. Rev. C **93**, 014911 (2016).

[76] J. Aichelin and K. Werner, Centrality dependence of strangeness enhancement in ultrarelativistic heavy ion collisions: A core-corona Effect, Phys. Rev. C **79**, 064907 (2009); **81**, 029902(E) (2010).

S. Acharya,[139] F. T.-. Acosta,[20] D. Adamová,[93] A. Adler,[74] J. Adolfsson,[80] M. M. Aggarwal,[98] G. Aglieri Rinella,[34] M. Agnello,[31] N. Agrawal,[48] Z. Ahammed,[139] S. U. Ahn,[76] S. Aiola,[144] A. Akindinov,[64] M. Al-Turany,[104] S. N. Alam,[139] D. S. D. Albuquerque,[121] D. Aleksandrov,[87] B. Alessandro,[58] H. M. Alfanda,[6] R. Alfaro Molina,[72] Y. Ali,[15] A. Alici,[10,27,53] A. Alkin,[2] J. Alme,[22] T. Alt,[69] L. Altenkamper,[22] I. Altsybeev,[111] M. N. Anaam,[6] C. Andrei,[47] D. Andreou,[34]

H. A. Andrews,[108] A. Andronic,[104,142] M. Angeletti,[34] V. Anguelov,[102] C. Anson,[16] T. Antičić,[105] F. Antinori,[56] P. Antonioli,[53] R. Anwar,[125] N. Apadula,[79] L. Aphecetche,[113] H. Appelshäuser,[69] S. Arcelli,[27] R. Arnaldi,[58] I. C. Arsene,[21] M. Arslandok,[102] A. Augustinus,[34] R. Averbeck,[104] M. D. Azmi,[17] A. Badalà,[55] Y. W. Baek,[40,60] S. Bagnasco,[58] R. Bailhache,[69] R. Bala,[99] A. Baldisseri,[135] M. Ball,[42] R. C. Baral,[85] A. M. Barbano,[26] R. Barbera,[28] F. Barile,[52] L. Barioglio,[26] G. G. Barnaföldi,[143] L. S. Barnby,[92] V. Barret,[132] P. Bartalini,[6] K. Barth,[34] E. Bartsch,[69] N. Bastid,[132] S. Basu,[141] G. Batigne,[113] B. Batyunya,[75] P. C. Batzing,[21] J. L. Bazo Alba,[109] I. G. Bearden,[88] H. Beck,[102] C. Bedda,[63] N. K. Behera,[60] I. Belikov,[134] F. Bellini,[34] H. Bello Martinez,[44] R. Bellwied,[125] L. G. E. Beltran,[119] V. Belyaev,[91] G. Bencedi,[143] S. Beole,[26] A. Bercuci,[47] Y. Berdnikov,[96] D. Berenyi,[143] R. A. Bertens,[128] D. Berzano,[34,58] L. Betev,[34] P. P. Bhaduri,[139] A. Bhasin,[99] I. R. Bhat,[99] H. Bhatt,[48] B. Bhattacharjee,[41] J. Bhom,[117] A. Bianchi,[26] L. Bianchi,[125] N. Bianchi,[51] J. Bielčík,[37] J. Bielčíková,[93] A. Bilandzic,[103,116] G. Biro,[143] R. Biswas,[3] S. Biswas,[3] J. T. Blair,[118] D. Blau,[87] C. Blume,[69] G. Boca,[137] F. Bock,[34] A. Bogdanov,[91] L. Boldizsár,[143] A. Bolozdynya,[91] M. Bombara,[38] G. Bonomi,[138] M. Bonora,[34] H. Borel,[135] A. Borissov,[102,142] M. Borri,[127] E. Botta,[26] C. Bourjau,[88] L. Bratrud,[69] P. Braun-Munzinger,[104] M. Bregant,[120] T. A. Broker,[69] M. Broz,[37] E. J. Brucken,[43] E. Bruna,[58] G. E. Bruno,[33,34] D. Budnikov,[106] H. Buesching,[69] S. Bufalino,[31] P. Buhler,[112] P. Buncic,[34] O. Busch,[131,a] Z. Buthelezi,[73] J. B. Butt,[15] J. T. Buxton,[95] J. Cabala,[115] D. Caffarri,[89] H. Caines,[144] A. Caliva,[104] E. Calvo Villar,[109] R. S. Camacho,[44] P. Camerini,[25] A. A. Capon,[112] W. Carena,[34] F. Carnesecchi,[10,27] J. Castillo Castellanos,[135] A. J. Castro,[128] E. A. R. Casula,[54] C. Ceballos Sanchez,[8] S. Chandra,[139] B. Chang,[126] W. Chang,[6] S. Chapeland,[34] M. Chartier,[127] S. Chattopadhyay,[139] S. Chattopadhyay,[107] A. Chauvin,[24] C. Cheshkov,[133] B. Cheynis,[133] V. Chibante Barroso,[34] D. D. Chinellato,[121] S. Cho,[60] P. Chochula,[34] T. Chowdhury,[132] P. Christakoglou,[89] C. H. Christensen,[88] P. Christiansen,[80] T. Chujo,[131] S. U. Chung,[18] C. Cicalo,[54] L. Cifarelli,[10,27] F. Cindolo,[53] J. Cleymans,[124] F. Colamaria,[52] D. Colella,[52] A. Collu,[79] M. Colocci,[27] M. Concas,[58,b] G. Conesa Balbastre,[78] Z. Conesa del Valle,[61] J. G. Contreras,[37] T. M. Cormier,[94] Y. Corrales Morales,[58] P. Cortese,[32] M. R. Cosentino,[122] F. Costa,[34] S. Costanza,[137] J. Crkovská,[61] P. Crochet,[132] E. Cuautle,[70] L. Cunqueiro,[94,142] T. Dahms,[103,116] A. Dainese,[56] F. P. A. Damas,[113,135] S. Dani,[66] M. C. Danisch,[102] A. Danu,[68] D. Das,[107] I. Das,[107] S. Das,[3] A. Dash,[85] S. Dash,[48] S. De,[49] A. De Caro,[30] G. de Cataldo,[52] C. de Conti,[120] J. de Cuveland,[39] A. De Falco,[24] D. De Gruttola,[10,30] N. De Marco,[58] S. De Pasquale,[30] R. D. De Souza,[121] H. F. Degenhardt,[120] A. Deisting,[102,104] A. Deloff,[84] S. Delsanto,[26] C. Deplano,[89] P. Dhankher,[48] D. Di Bari,[33] A. Di Mauro,[34] B. Di Ruzza,[56] R. A. Diaz,[8] T. Dietel,[124] P. Dillenseger,[69] Y. Ding,[6] R. Divià,[34] Ø. Djuvsland,[22] A. Dobrin,[34] D. Domenicis Gimenez,[120] B. Dönigus,[69] O. Dordic,[21] A. K. Dubey,[139] A. Dubla,[104] L. Ducroux,[133] S. Dudi,[98] A. K. Duggal,[98] M. Dukhishyam,[85] P. Dupieux,[132] R. J. Ehlers,[144] D. Elia,[52] E. Endress,[109] H. Engel,[74] E. Epple,[144] B. Erazmus,[113] F. Erhardt,[97] M. R. Ersdal,[22] B. Espagnon,[61] G. Eulisse,[34] J. Eum,[18] D. Evans,[108] S. Evdokimov,[90] L. Fabbietti,[103,116] M. Faggin,[29] J. Faivre,[78] A. Fantoni,[51] M. Fasel,[94] L. Feldkamp,[142] A. Feliciello,[58] G. Feofilov,[111] A. Fernández Téllez,[44] A. Ferretti,[26] A. Festanti,[34] V. J. G. Feuillard,[102] J. Figiel,[117] M. A. S. Figueredo,[120] S. Filchagin,[106] D. Finogeev,[62] F. M. Fionda,[22] G. Fiorenza,[52] F. Flor,[125] M. Floris,[34] S. Foertsch,[73] P. Foka,[104] S. Fokin,[87] E. Fragiacomo,[59] A. Francescon,[34] A. Francisco,[113] U. Frankenfeld,[104] G. G. Fronze,[26] U. Fuchs,[34] C. Furget,[78] A. Furs,[62] M. Fusco Girard,[30] J. J. Gaardhøje,[88] M. Gagliardi,[26] A. M. Gago,[109] K. Gajdosova,[88] M. Gallio,[26] C. D. Galvan,[119] P. Ganoti,[83] C. Garabatos,[104] E. Garcia-Solis,[11] K. Garg,[28] C. Gargiulo,[34] P. Gasik,[103,116] E. F. Gauger,[118] M. B. Gay Ducati,[71] M. Germain,[113] J. Ghosh,[107] P. Ghosh,[139] S. K. Ghosh,[3] P. Gianotti,[51] P. Giubellino,[58,104] P. Giubilato,[29] P. Glässel,[102] D. M. Gomez Coral,[72] A. Gomez Ramirez,[74] V. Gonzalez,[104] P. González-Zamora,[44] S. Gorbunov,[39] L. Görlich,[117] S. Gotovac,[35] V. Grabski,[72] L. K. Graczykowski,[140] K. L. Graham,[108] L. Greiner,[79] A. Grelli,[63] C. Grigoras,[34] V. Grigoriev,[91] A. Grigoryan,[1] S. Grigoryan,[75] J. M. Gronefeld,[104] F. Grosa,[31] J. F. Grosse-Oetringhaus,[34] R. Grosso,[104] R. Guernane,[78] B. Guerzoni,[27] M. Guittiere,[113] K. Gulbrandsen,[88] T. Gunji,[130] A. Gupta,[99] R. Gupta,[99] I. B. Guzman,[44] R. Haake,[34,144] M. K. Habib,[104] C. Hadjidakis,[61] H. Hamagaki,[81] G. Hamar,[143] M. Hamid,[6] J. C. Hamon,[134] R. Hannigan,[118] M. R. Haque,[63] A. Harlenderova,[104] J. W. Harris,[144] A. Harton,[11] H. Hassan,[78] D. Hatzifotiadou,[10,53] S. Hayashi,[130] S. T. Heckel,[69] E. Hellbär,[69] H. Helstrup,[36] A. Herghelegiu,[47] E. G. Hernandez,[44] G. Herrera Corral,[9] F. Herrmann,[142] K. F. Hetland,[36] T. E. Hilden,[43] H. Hillemanns,[34] C. Hills,[127] B. Hippolyte,[134] B. Hohlweger,[103] D. Horak,[37] S. Hornung,[104] R. Hosokawa,[78,131] J. Hota,[66] P. Hristov,[34] C. Huang,[61] C. Hughes,[128] P. Huhn,[69] T. J. Humanic,[95] H. Hushnud,[107] N. Hussain,[41] T. Hussain,[17] D. Hutter,[39] D. S. Hwang,[19] J. P. Iddon,[127] R. Ilkaev,[106] M. Inaba,[131] M. Ippolitov,[87] M. S. Islam,[107] M. Ivanov,[104] V. Ivanov,[96] V. Izucheev,[90] B. Jacak,[79] N. Jacazio,[27] P. M. Jacobs,[79] M. B. Jadhav,[48] S. Jadlovska,[115] J. Jadlovsky,[115] S. Jaelani,[63] C. Jahnke,[116,120] M. J. Jakubowska,[140] M. A. Janik,[140] C. Jena,[85] M. Jercic,[97] O. Jevons,[108] R. T. Jimenez Bustamante,[104] M. Jin,[125] P. G. Jones,[108] A. Jusko,[108] P. Kalinak,[65] A. Kalweit,[34] J. H. Kang,[145] V. Kaplin,[91] S. Kar,[6] A. Karasu Uysal,[77] O. Karavichev,[62] T. Karavicheva,[62] P. Karczmarczyk,[34] E. Karpechev,[62] U. Kebschull,[74] R. Keidel,[46] D. L. D. Keijdener,[63] M. Keil,[34] B. Ketzer,[42] Z. Khabanova,[89] A. M. Khan,[6] S. Khan,[17] S. A. Khan,[139] A. Khanzadeev,[96] Y. Kharlov,[90] A. Khatun,[17] A. Khuntia,[49] M. M. Kielbowicz,[117] B. Kileng,[36] B. Kim,[131] D. Kim,[145] D. J. Kim,[126] E. J. Kim,[13] H. Kim,[145] J. S. Kim,[40] J. Kim,[102] J. Kim,[13] M. Kim,[60,102] S. Kim,[19] T. Kim,[145] T. Kim,[145] K. Kindra,[98] S. Kirsch,[39] I. Kisel,[39] S. Kiselev,[64] A. Kisiel,[140] J. L. Klay,[5] C. Klein,[69] J. Klein,[58] C. Klein-Bösing,[142] S. Klewin,[102] A. Kluge,[34] M. L. Knichel,[34] A. G. Knospe,[125] C. Kobdaj,[114] M. Kofarago,[143] M. K. Köhler,[102] T. Kollegger,[104] N. Kondratyeva,[91] E. Kondratyuk,[90] A. Konevskikh,[62] P. J. Konopka,[34] M. Konyushikhin,[141] L. Koska,[115] O. Kovalenko,[84] V. Kovalenko,[111] M. Kowalski,[117] I. Králik,[65] A. Kravčáková,[38] L. Kreis,[104] M. Krivda,[65,108] F. Krizek,[93] M. Krüger,[69] E. Kryshen,[96] M. Krzewicki,[39] A. M. Kubera,[95] V. Kučera,[60,93] C. Kuhn,[134] P. G. Kuijer,[89] J. Kumar,[48] L. Kumar,[98] S. Kumar,[48] S. Kundu,[85] P. Kurashvili,[84] A. Kurepin,[62] A. B. Kurepin,[62] S. Kushpil,[93] J. Kvapil,[108] M. J. Kweon,[60] Y. Kwon,[145]

S. L. La Pointe,[39] P. La Rocca,[28] Y. S. Lai,[79] I. Lakomov,[34] R. Langoy,[123] K. Lapidus,[144] A. Lardeux,[21] P. Larionov,[51] E. Laudi,[34] R. Lavicka,[37] R. Lea,[25] L. Leardini,[102] S. Lee,[145] F. Lehas,[89] S. Lehner,[112] J. Lehrbach,[39] R. C. Lemmon,[92] I. León Monzón,[119] P. Lévai,[143] X. Li,[12] X. L. Li,[6] J. Lien,[123] R. Lietava,[108] B. Lim,[18] S. Lindal,[21] V. Lindenstruth,[39] S. W. Lindsay,[127] C. Lippmann,[104] M. A. Lisa,[95] V. Litichevskyi,[43] A. Liu,[79] H. M. Ljunggren,[80] W. J. Llope,[141] D. F. Lodato,[63] V. Loginov,[91] C. Loizides,[79,94] P. Loncar,[35] X. Lopez,[132] E. López Torres,[8] P. Luettig,[69] J. R. Luhder,[142] M. Lunardon,[29] G. Luparello,[59] M. Lupi,[34] A. Maevskaya,[62] M. Mager,[34] S. M. Mahmood,[21] A. Maire,[134] R. D. Majka,[144] M. Malaev,[96] Q. W. Malik,[21] L. Malinina,[75,c] D. Mal'Kevich,[64] P. Malzacher,[104] A. Mamonov,[106] V. Manko,[87] F. Manso,[132] V. Manzari,[52] Y. Mao,[6] M. Marchisone,[129,133] J. Mareš,[67] G. V. Margagliotti,[25] A. Margotti,[53] J. Margutti,[63] A. Marín,[104] C. Markert,[118] M. Marquard,[69] N. A. Martin,[102,104] P. Martinengo,[34] J. L. Martinez,[125] M. I. Martínez,[44] G. Martínez García,[113] M. Martinez Pedreira,[34] S. Masciocchi,[104] M. Masera,[26] A. Masoni,[54] L. Massacrier,[61] E. Masson,[113] A. Mastroserio,[52,136] A. M. Mathis,[103,116] P. F. T. Matuoka,[120] A. Matyja,[117,128] C. Mayer,[117] M. Mazzilli,[33] M. A. Mazzoni,[57] F. Meddi,[23] Y. Melikyan,[91] A. Menchaca-Rocha,[72] E. Meninno,[30] M. Meres,[14] S. Mhlanga,[124] Y. Miake,[131] L. Micheletti,[26] M. M. Mieskolainen,[43] D. L. Mihaylov,[103] K. Mikhaylov,[64,75] A. Mischke,[63] A. N. Mishra,[70] D. Miśkowiec,[104] J. Mitra,[139] C. M. Mitu,[68] N. Mohammadi,[34] A. P. Mohanty,[63] B. Mohanty,[85] M. Mohisin Khan,[17,d] D. A. Moreira De Godoy,[142] L. A. P. Moreno,[44] S. Moretto,[29] A. Morreale,[113] A. Morsch,[34] T. Mrnjavac,[34] V. Muccifora,[51] E. Mudnic,[35] D. Mühlheim,[142] S. Muhuri,[139] M. Mukherjee,[3] J. D. Mulligan,[144] M. G. Munhoz,[120] K. Münning,[42] M. I. A. Munoz,[79] R. H. Munzer,[69] H. Murakami,[130] S. Murray,[73] L. Musa,[34] J. Musinsky,[65] C. J. Myers,[125] J. W. Myrcha,[140] B. Naik,[48] R. Nair,[84] B. K. Nandi,[48] R. Nania,[10,53] E. Nappi,[52] A. Narayan,[48] M. U. Naru,[15] A. F. Nassirpour,[80] H. Natal da Luz,[120] C. Nattrass,[128] S. R. Navarro,[44] K. Nayak,[85] R. Nayak,[48] T. K. Nayak,[139] S. Nazarenko,[106] R. A. Negrao De Oliveira,[34,69] L. Nellen,[70] S. V. Nesbo,[36] G. Neskovic,[39] F. Ng,[125] M. Nicassio,[104] J. Niedziela,[34,140] B. S. Nielsen,[88] S. Nikolaev,[87] S. Nikulin,[87] V. Nikulin,[96] F. Noferini,[10,53] P. Nomokonov,[75] G. Nooren,[63] J. C. C. Noris,[44] J. Norman,[78] A. Nyanin,[87] J. Nystrand,[22] M. Ogino,[81] H. Oh,[145] A. Ohlson,[102] J. Oleniacz,[140] A. C. Oliveira Da Silva,[120] M. H. Oliver,[144] J. Onderwaater,[104] C. Oppedisano,[58] R. Orava,[43] M. Oravec,[115] A. Ortiz Velasquez,[70] A. Oskarsson,[80] J. Otwinowski,[117] K. Oyama,[81] Y. Pachmayer,[102] V. Pacik,[88] D. Pagano,[138] G. Paić,[70] P. Palni,[6] J. Pan,[141] A. K. Pandey,[48] S. Panebianco,[135] V. Papikyan,[1] P. Pareek,[49] J. Park,[60] J. E. Parkkila,[126] S. Parmar,[98] A. Passfeld,[142] S. P. Pathak,[125] R. N. Patra,[139] B. Paul,[58] H. Pei,[6] T. Peitzmann,[63] X. Peng,[6] L. G. Pereira,[71] H. Pereira Da Costa,[135] D. Peresunko,[87] E. Perez Lezama,[69] V. Peskov,[69] Y. Pestov,[4] V. Petráček,[37] M. Petrovici,[47] C. Petta,[28] R. P. Pezzi,[71] S. Piano,[59] M. Pikna,[14] P. Pillot,[113] L. O. D. L. Pimentel,[88] O. Pinazza,[34,53] L. Pinsky,[125] S. Pisano,[51] D. B. Piyarathna,[125] M. Płoskoń,[79] M. Planinic,[97] F. Pliquett,[69] J. Pluta,[140] S. Pochybova,[143] P. L. M. Podesta-Lerma,[119] M. G. Poghosyan,[94] B. Polichtchouk,[90] N. Poljak,[97] W. Poonsawat,[114] A. Pop,[47] H. Poppenborg,[142] S. Porteboeuf-Houssais,[132] V. Pozdniakov,[75] S. K. Prasad,[3] R. Preghenella,[53] F. Prino,[58] C. A. Pruneau,[141] I. Pshenichnov,[62] M. Puccio,[26] V. Punin,[106] K. Puranapanda,[139] J. Putschke,[141] S. Raha,[3] S. Rajput,[99] J. Rak,[126] A. Rakotozafindrabe,[135] L. Ramello,[32] F. Rami,[134] R. Raniwala,[100] S. Raniwala,[100] S. S. Räsänen,[43] B. T. Rascanu,[69] R. Rath,[49] V. Ratza,[42] I. Ravasenga,[31] K. F. Read,[94,128] K. Redlich,[84,e] A. Rehman,[22] P. Reichelt,[69] F. Reidt,[34] X. Ren,[6] R. Renfordt,[69] A. Reshetin,[62] J.-P. Revol,[10] K. Reygers,[102] V. Riabov,[96] T. Richert,[63,80,88] M. Richter,[21] P. Riedler,[34] W. Riegler,[34] F. Riggi,[28] C. Ristea,[68] S. P. Rode,[49] M. Rodríguez Cahuantzi,[44] K. Røed,[21] R. Rogalev,[90] E. Rogochaya,[75] D. Rohr,[34] D. Röhrich,[22] P. S. Rokita,[140] F. Ronchetti,[51] E. D. Rosas,[70] K. Roslon,[140] P. Rosnet,[132] A. Rossi,[29,56] A. Rotondi,[137] F. Roukoutakis,[83] C. Roy,[134] P. Roy,[107] O. V. Rueda,[70] R. Rui,[25] B. Rumyantsev,[75] A. Rustamov,[86] E. Ryabinkin,[87] Y. Ryabov,[96] A. Rybicki,[117] S. Saarinen,[43] S. Sadhu,[139] S. Sadovsky,[90] K. Šafařík,[34] S. K. Saha,[139] B. Sahoo,[48] P. Sahoo,[49] R. Sahoo,[49] S. Sahoo,[66] P. K. Sahu,[66] J. Saini,[139] S. Sakai,[131] M. A. Saleh,[141] S. Sambyal,[99] V. Samsonov,[91,96] A. Sandoval,[72] A. Sarkar,[73] D. Sarkar,[139] N. Sarkar,[139] P. Sarma,[41] M. H. P. Sas,[63] E. Scapparone,[53] F. Scarlassara,[29] B. Schaefer,[94] H. S. Scheid,[69] C. Schiaua,[47] R. Schicker,[102] C. Schmidt,[104] H. R. Schmidt,[101] M. O. Schmidt,[102] M. Schmidt,[101] N. V. Schmidt,[69,94] J. Schukraft,[34] Y. Schutz,[34,134] K. Schwarz,[104] K. Schweda,[104] G. Scioli,[27] E. Scomparin,[58] M. Šefčík,[38] J. E. Seger,[16] Y. Sekiguchi,[130] D. Sekihata,[45] I. Selyuzhenkov,[91,104] S. Senyukov,[134] E. Serradilla,[72] P. Sett,[48] A. Sevcenco,[68] A. Shabanov,[62] A. Shabetai,[113] R. Shahoyan,[34] W. Shaikh,[107] A. Shangaraev,[90] A. Sharma,[98] A. Sharma,[99] M. Sharma,[99] N. Sharma,[98] A. I. Sheikh,[139] K. Shigaki,[45] M. Shimomura,[82] S. Shirinkin,[64] Q. Shou,[6,110] Y. Sibiriak,[87] S. Siddhanta,[54] K. M. Sielewicz,[34] T. Siemiarczuk,[84] D. Silvermyr,[80] G. Simatovic,[89] G. Simonetti,[34,103] R. Singaraju,[139] R. Singh,[85] R. Singh,[99] V. Singhal,[139] T. Sinha,[107] B. Sitar,[14] M. Sitta,[32] T. B. Skaali,[21] M. Slupecki,[126] N. Smirnov,[144] R. J. M. Snellings,[63] T. W. Snellman,[126] J. Sochan,[115] C. Soncco,[109] J. Song,[18] A. Songmoolnak,[114] F. Soramel,[29] S. Sorensen,[128] F. Sozzi,[104] I. Sputowska,[117] J. Stachel,[102] I. Stan,[68] P. Stankus,[94] E. Stenlund,[80] D. Stocco,[113] M. M. Storetvedt,[36] P. Strmen,[14] A. A. P. Suaide,[120] T. Sugitate,[45] C. Suire,[61] M. Suleymanov,[15] M. Suljic,[34] R. Sultanov,[64] M. Šumbera,[93] S. Sumowidagdo,[50] K. Suzuki,[112] S. Swain,[66] A. Szabo,[14] I. Szarka,[14] U. Tabassam,[15] J. Takahashi,[121] G. J. Tambave,[22] N. Tanaka,[131] M. Tarhini,[113] M. G. Tarzila,[47] A. Tauro,[34] G. Tejeda Muñoz,[44] A. Telesca,[34] C. Terrevoli,[29] B. Teyssier,[133] D. Thakur,[49] S. Thakur,[139] D. Thomas,[118] F. Thoresen,[88] R. Tieulent,[133] A. Tikhonov,[62] A. R. Timmins,[125] A. Toia,[69] N. Topilskaya,[62] M. Toppi,[51] S. R. Torres,[119] S. Tripathy,[49] S. Trogolo,[26] G. Trombetta,[33] L. Tropp,[38] V. Trubnikov,[2] W. H. Trzaska,[126] T. P. Trzcinski,[140] B. A. Trzeciak,[63] T. Tsuji,[130] A. Tumkin,[106] R. Turrisi,[56] T. S. Tveter,[21] K. Ullaland,[22] E. N. Umaka,[125] A. Uras,[133] G. L. Usai,[24] A. Utrobicic,[97] M. Vala,[115] L. Valencia Palomo,[44] N. Valle,[137] N. van der Kolk,[63] L. V. R. van Doremalen,[63] J. W. Van Hoorne,[34] M. van Leeuwen,[63] P. Vande Vyvre,[34] D. Varga,[143] A. Vargas,[44] M. Vargyas,[126] R. Varma,[48] M. Vasileiou,[83] A. Vasiliev,[87] O. Vázquez Doce,[103,116] V. Vechernin,[111] A. M. Veen,[63] E. Vercellin,[26] S. Vergara Limón,[44] L. Vermunt,[63] R. Vernet,[7] R. Vértesi,[143] L. Vickovic,[35]

J. Viinikainen,[126] Z. Vilakazi,[129] O. Villalobos Baillie,[108] A. Villatoro Tello,[44] A. Vinogradov,[87] T. Virgili,[30] V. Vislavicius,[80,88] A. Vodopyanov,[75] M. A. Völkl,[101] K. Voloshin,[64] S. A. Voloshin,[141] G. Volpe,[33] B. von Haller,[34] I. Vorobyev,[103,116] D. Voscek,[115] D. Vranic,[34,104] J. Vrláková,[38] B. Wagner,[22] M. Wang,[6] Y. Watanabe,[131] M. Weber,[112] S. G. Weber,[104] A. Wegrzynek,[34] D. F. Weiser,[102] S. C. Wenzel,[34] J. P. Wessels,[142] U. Westerhoff,[142] A. M. Whitehead,[124] J. Wiechula,[69] J. Wikne,[21] G. Wilk,[84] J. Wilkinson,[53] G. A. Willems,[34,142] M. C. S. Williams,[53] E. Willsher,[108] B. Windelband,[102] W. E. Witt,[128] R. Xu,[6] S. Yalcin,[77] K. Yamakawa,[45] S. Yano,[45,135] Z. Yin,[6] H. Yokoyama,[78,131] I.-K. Yoo,[18] J. H. Yoon,[60] S. Yuan,[22] V. Yurchenko,[2] V. Zaccolo,[58] A. Zaman,[15] C. Zampolli,[34] H. J. C. Zanoli,[120] N. Zardoshti,[108] A. Zarochentsev,[111] P. Závada,[67] N. Zaviyalov,[106] H. Zbroszczyk,[140] M. Zhalov,[96] X. Zhang,[6] Y. Zhang,[6] Z. Zhang,[6,132] C. Zhao,[21] V. Zherebchevskii,[111] N. Zhigareva,[64] D. Zhou,[6] Y. Zhou,[88] Z. Zhou,[22] H. Zhu,[6] J. Zhu,[6] Y. Zhu,[6] A. Zichichi,[10,27] M. B. Zimmermann,[34] G. Zinovjev,[2] and J. Zmeskal[112]

(ALICE Collaboration)

[1]*A. I. Alikhanyan National Science Laboratory (Yerevan Physics Institute) Foundation, Yerevan, Armenia*
[2]*Bogolyubov Institute for Theoretical Physics, National Academy of Sciences of Ukraine, Kiev, Ukraine*
[3]*Bose Institute, Department of Physics and Centre for Astroparticle Physics and Space Science (CAPSS), Kolkata, India*
[4]*Budker Institute for Nuclear Physics, Novosibirsk, Russia*
[5]*California Polytechnic State University, San Luis Obispo, California, USA*
[6]*Central China Normal University, Wuhan, China*
[7]*Centre de Calcul de l'IN2P3, Villeurbanne, Lyon, France*
[8]*Centro de Aplicaciones Tecnológicas y Desarrollo Nuclear (CEADEN), Havana, Cuba*
[9]*Centro de Investigación y de Estudios Avanzados (CINVESTAV), Mexico City and Mérida, Mexico*
[10]*Centro Fermi - Museo Storico della Fisica e Centro Studi e Ricerche "Enrico Fermi", Rome, Italy*
[11]*Chicago State University, Chicago, Illinois, USA*
[12]*China Institute of Atomic Energy, Beijing, China*
[13]*Chonbuk National University, Jeonju, Republic of Korea*
[14]*Comenius University Bratislava, Faculty of Mathematics, Physics and Informatics, Bratislava, Slovakia*
[15]*COMSATS Institute of Information Technology (CIIT), Islamabad, Pakistan*
[16]*Creighton University, Omaha, Nebraska, USA*
[17]*Department of Physics, Aligarh Muslim University, Aligarh, India*
[18]*Department of Physics, Pusan National University, Pusan, Republic of Korea*
[19]*Department of Physics, Sejong University, Seoul, Republic of Korea*
[20]*Department of Physics, University of California, Berkeley, California, USA*
[21]*Department of Physics, University of Oslo, Oslo, Norway*
[22]*Department of Physics and Technology, University of Bergen, Bergen, Norway*
[23]*Dipartimento di Fisica dell'Università "La Sapienza" and Sezione INFN, Rome, Italy*
[24]*Dipartimento di Fisica dell'Università and Sezione INFN, Cagliari, Italy*
[25]*Dipartimento di Fisica dell'Università and Sezione INFN, Trieste, Italy*
[26]*Dipartimento di Fisica dell'Università and Sezione INFN, Turin, Italy*
[27]*Dipartimento di Fisica e Astronomia dell'Università and Sezione INFN, Bologna, Italy*
[28]*Dipartimento di Fisica e Astronomia dell'Università and Sezione INFN, Catania, Italy*
[29]*Dipartimento di Fisica e Astronomia dell'Università and Sezione INFN, Padova, Italy*
[30]*Dipartimento di Fisica 'E. R. Caianiello' dell'Università and Gruppo Collegato INFN, Salerno, Italy*
[31]*Dipartimento DISAT del Politecnico and Sezione INFN, Turin, Italy*
[32]*Dipartimento di Scienze e Innovazione Tecnologica dell'Università del Piemonte Orientale and INFN Sezione di Torino, Alessandria, Italy*
[33]*Dipartimento Interateneo di Fisica "M. Merlin" and Sezione INFN, Bari, Italy*
[34]*European Organization for Nuclear Research (CERN), Geneva, Switzerland*
[35]*Faculty of Electrical Engineering, Mechanical Engineering and Naval Architecture, University of Split, Split, Croatia*
[36]*Faculty of Engineering and Science, Western Norway University of Applied Sciences, Bergen, Norway*
[37]*Faculty of Nuclear Sciences and Physical Engineering, Czech Technical University in Prague, Prague, Czech Republic*
[38]*Faculty of Science, P. J. Šafárik University, Košice, Slovakia*
[39]*Frankfurt Institute for Advanced Studies, Johann Wolfgang Goethe-Universität Frankfurt, Frankfurt, Germany*
[40]*Gangneung-Wonju National University, Gangneung, Republic of Korea*
[41]*Gauhati University, Department of Physics, Guwahati, India*
[42]*Helmholtz-Institut für Strahlen- und Kernphysik, Rheinische Friedrich-Wilhelms-Universität Bonn, Bonn, Germany*
[43]*Helsinki Institute of Physics (HIP), Helsinki, Finland*
[44]*High Energy Physics Group, Universidad Autónoma de Puebla, Puebla, Mexico*
[45]*Hiroshima University, Hiroshima, Japan*

[46]*Hochschule Worms, Zentrum für Technologietransfer und Telekommunikation (ZTT), Worms, Germany*
[47]*Horia Hulubei National Institute of Physics and Nuclear Engineering, Bucharest, Romania*
[48]*Indian Institute of Technology Bombay (IIT), Mumbai, India*
[49]*Indian Institute of Technology Indore, Indore, India*
[50]*Indonesian Institute of Sciences, Jakarta, Indonesia*
[51]*INFN, Laboratori Nazionali di Frascati, Frascati, Italy*
[52]*INFN, Sezione di Bari, Bari, Italy*
[53]*INFN, Sezione di Bologna, Bologna, Italy*
[54]*INFN, Sezione di Cagliari, Cagliari, Italy*
[55]*INFN, Sezione di Catania, Catania, Italy*
[56]*INFN, Sezione di Padova, Padova, Italy*
[57]*INFN, Sezione di Roma, Rome, Italy*
[58]*INFN, Sezione di Torino, Turin, Italy*
[59]*INFN, Sezione di Trieste, Trieste, Italy*
[60]*Inha University, Incheon, Republic of Korea*
[61]*Institut de Physique Nucléaire d'Orsay (IPNO), Institut National de Physique Nucléaire et de Physique des Particules (IN2P3/CNRS), Université de Paris-Sud, Université Paris-Saclay, Orsay, France*
[62]*Institute for Nuclear Research, Academy of Sciences, Moscow, Russia*
[63]*Institute for Subatomic Physics, Utrecht University/Nikhef, Utrecht, Netherlands*
[64]*Institute for Theoretical and Experimental Physics, Moscow, Russia*
[65]*Institute of Experimental Physics, Slovak Academy of Sciences, Košice, Slovakia*
[66]*Institute of Physics, Homi Bhabha National Institute, Bhubaneswar, India*
[67]*Institute of Physics of the Czech Academy of Sciences, Prague, Czech Republic*
[68]*Institute of Space Science (ISS), Bucharest, Romania*
[69]*Institut für Kernphysik, Johann Wolfgang Goethe-Universität Frankfurt, Frankfurt, Germany*
[70]*Instituto de Ciencias Nucleares, Universidad Nacional Autónoma de México, Mexico City, Mexico*
[71]*Instituto de Física, Universidade Federal do Rio Grande do Sul (UFRGS), Porto Alegre, Brazil*
[72]*Instituto de Física, Universidad Nacional Autónoma de México, Mexico City, Mexico*
[73]*iThemba LABS, National Research Foundation, Somerset West, South Africa*
[74]*Johann-Wolfgang-Goethe Universität Frankfurt Institut für Informatik, Fachbereich Informatik und Mathematik, Frankfurt, Germany*
[75]*Joint Institute for Nuclear Research (JINR), Dubna, Russia*
[76]*Korea Institute of Science and Technology Information, Daejeon, Republic of Korea*
[77]*KTO Karatay University, Konya, Turkey*
[78]*Laboratoire de Physique Subatomique et de Cosmologie, Université Grenoble-Alpes, CNRS-IN2P3, Grenoble, France*
[79]*Lawrence Berkeley National Laboratory, Berkeley, California, USA*
[80]*Lund University Department of Physics, Division of Particle Physics, Lund, Sweden*
[81]*Nagasaki Institute of Applied Science, Nagasaki, Japan*
[82]*Nara Women's University (NWU), Nara, Japan*
[83]*National and Kapodistrian University of Athens, School of Science, Department of Physics, Athens, Greece*
[84]*National Centre for Nuclear Research, Warsaw, Poland*
[85]*National Institute of Science Education and Research, Homi Bhabha National Institute, Jatni, India*
[86]*National Nuclear Research Center, Baku, Azerbaijan*
[87]*National Research Centre Kurchatov Institute, Moscow, Russia*
[88]*Niels Bohr Institute, University of Copenhagen, Copenhagen, Denmark*
[89]*Nikhef, National institute for subatomic physics, Amsterdam, Netherlands*
[90]*NRC Kurchatov Institute IHEP, Protvino, Russia*
[91]*NRNU Moscow Engineering Physics Institute, Moscow, Russia*
[92]*Nuclear Physics Group, STFC Daresbury Laboratory, Daresbury, United Kingdom*
[93]*Nuclear Physics Institute of the Czech Academy of Sciences, Řež u Prahy, Czech Republic*
[94]*Oak Ridge National Laboratory, Oak Ridge, Tennessee, USA*
[95]*Ohio State University, Columbus, Ohio, USA*
[96]*Petersburg Nuclear Physics Institute, Gatchina, Russia*
[97]*Physics department, Faculty of science, University of Zagreb, Zagreb, Croatia*
[98]*Physics Department, Panjab University, Chandigarh, India*
[99]*Physics Department, University of Jammu, Jammu, India*
[100]*Physics Department, University of Rajasthan, Jaipur, India*
[101]*Physikalisches Institut, Eberhard-Karls-Universität Tübingen, Tübingen, Germany*
[102]*Physikalisches Institut, Ruprecht-Karls-Universität Heidelberg, Heidelberg, Germany*
[103]*Physik Department, Technische Universität München, Munich, Germany*

[104]*Research Division and ExtreMe Matter Institute EMMI, GSI Helmholtzzentrum für Schwerionenforschung GmbH, Darmstadt, Germany*
[105]*Rudjer Bošković Institute, Zagreb, Croatia*
[106]*Russian Federal Nuclear Center (VNIIEF), Sarov, Russia*
[107]*Saha Institute of Nuclear Physics, Homi Bhabha National Institute, Kolkata, India*
[108]*School of Physics and Astronomy, University of Birmingham, Birmingham, United Kingdom*
[109]*Sección Física, Departamento de Ciencias, Pontificia Universidad Católica del Perú, Lima, Peru*
[110]*Shanghai Institute of Applied Physics, Shanghai, China*
[111]*St. Petersburg State University, St. Petersburg, Russia*
[112]*Stefan Meyer Institut für Subatomare Physik (SMI), Vienna, Austria*
[113]*SUBATECH, IMT Atlantique, Université de Nantes, CNRS-IN2P3, Nantes, France*
[114]*Suranaree University of Technology, Nakhon Ratchasima, Thailand*
[115]*Technical University of Košice, Košice, Slovakia*
[116]*Technische Universität München, Excellence Cluster "Universe," Munich, Germany*
[117]*The Henryk Niewodniczanski Institute of Nuclear Physics, Polish Academy of Sciences, Cracow, Poland*
[118]*The University of Texas at Austin, Austin, Texas, USA*
[119]*Universidad Autónoma de Sinaloa, Culiacán, Mexico*
[120]*Universidade de São Paulo (USP), São Paulo, Brazil*
[121]*Universidade Estadual de Campinas (UNICAMP), Campinas, Brazil*
[122]*Universidade Federal do ABC, Santo Andre, Brazil*
[123]*University College of Southeast Norway, Tonsberg, Norway*
[124]*University of Cape Town, Cape Town, South Africa*
[125]*University of Houston, Houston, Texas, USA*
[126]*University of Jyväskylä, Jyväskylä, Finland*
[127]*University of Liverpool, Liverpool, United Kingdom*
[128]*University of Tennessee, Knoxville, Tennessee, USA*
[129]*University of the Witwatersrand, Johannesburg, South Africa*
[130]*University of Tokyo, Tokyo, Japan*
[131]*University of Tsukuba, Tsukuba, Japan*
[132]*Université Clermont Auvergne, CNRS/IN2P3, LPC, Clermont-Ferrand, France*
[133]*Université de Lyon, Université Lyon 1, CNRS/IN2P3, IPN-Lyon, Villeurbanne, Lyon, France*
[134]*Université de Strasbourg, CNRS, IPHC UMR 7178, F-67000 Strasbourg, France, Strasbourg, France*
[135]*Université Paris-Saclay Centre dÉtudes de Saclay (CEA), IRFU, Department de Physique Nucléaire (DPhN), Saclay, France*
[136]*Università degli Studi di Foggia, Foggia, Italy*
[137]*Università degli Studi di Pavia and Sezione INFN, Pavia, Italy*
[138]*Università di Brescia and Sezione INFN, Brescia, Italy*
[139]*Variable Energy Cyclotron Centre, Homi Bhabha National Institute, Kolkata, India*
[140]*Warsaw University of Technology, Warsaw, Poland*
[141]*Wayne State University, Detroit, Michigan, USA*
[142]*Westfälische Wilhelms-Universität Münster, Institut für Kernphysik, Münster, Germany*
[143]*Wigner Research Centre for Physics, Hungarian Academy of Sciences, Budapest, Hungary*
[144]*Yale University, New Haven, Connecticut, USA*
[145]*Yonsei University, Seoul, Republic of Korea*

[a]Deceased.
[b]Also at: Dipartimento DET del Politecnico di Torino, Turin, Italy.
[c]Also at: M. V. Lomonosov Moscow State University, D. V. Skobeltsyn Institute of Nuclear, Physics, Moscow, Russia.
[d]Also at: Department of Applied Physics, Aligarh Muslim University, Aligarh, India.
[e]Also at: Institute of Theoretical Physics, University of Wroclaw, Poland.